IMPROVEMENT OF THERMOELECTRIC OXIDES FOR A SIMPLE THERMOELECTRIC GENERATOR

BY

Claire Dvorak

A THESIS
SUBMITTED TO THE FACULTY OF

ALFRED UNIVERSITY

IN PARTIAL FULFILLMENT OF THE REQUIREMENTS
FOR THE DEGREE OF

MASTER OF SCIENCE

IN

CERAMIC ENGINEERING

ALFRED, NEW YORK

SEPTEMBER, 2015

IMPROVEMENT OF THERMOELECTRIC OXIDES IN FOR A SIMPLE THERMOELECTRIC GENERATOR

BY

CLAIRE DVORAK

B.S. ALFRED UNIVERSITY 2013

SIGNATURE OF AUTHOR_____

APPROVED BY_____

DOREEN D. EDWARDS, ADVISOR

_____

DAWEI LIU, ADVISORY COMMITTEE

_____

SCOTT T. MISTURE, ADVISORY COMMITTEE

_____

CHAIR, ORAL THESIS DEFENSE

ACCEPTED BY_____

DOREEN D. EDWARDS, DEAN
KAZUO INAMORI SCHOOL OF ENGINEERING

ACKNOWLEDGMENTS

There are a great many people who, without their assistance, I would not have completed this thesis. First I must acknowledge my advisor, Dr. Doreen Edwards, for all the great advice and guidance through the past two years and the entertaining trips to Albany. I would also like to thank my committee: Dr. Scott Misture, and Dr. Dawei Liu, for their expertise and insight on my thesis.

Next I need to thank those in my research group: Mike Alberga, Ana Fredell, and Brittany "Higgs" Higgins; without them I would not have gotten through the long nights of lab work, typing, and making presentations for conferences (Go Team Edwards!). A giant thank you to Gerry Wynick and Fran Williams for assistance in SEM and all things electronic. This work was sponsored in part by NYSERDA Agreement No 30370, and I would like to acknowledge those who I have worked with on this NYSERDA project: Dr. Mike Chu, Dr. Andy Hope, Dr. Robert Stevens, Dr. Eric Thatcher, and Dr. Venkatswaran Viswanathan. Also I need to thank Katie Decker and Tiffany Horton for all the assistance with paperwork, conferences, and scheduling meetings with Dr. Edwards; I would not have made any deadlines without those two wonderful ladies.

It is necessary for me to thank Zach and Rebecca Hamm, and the Bun for all the loads of laundry, dinners, and the use of a sledgehammer when necessary. I don't think I would have gotten through the past two years without their support here in Alfred. And finally, I would like to profusely thank my parents, Denny and Ellen, my sister, Katie, and my brother, Joe, for the endless support, many phone calls, and attempting to understand what I've been working on for the past two years.

TABLE OF CONTENTS

Page

Acknowledgments iv

Table of Contents v

List of Tables vii

List of Figures viii

Abstract xi

I. Introduction 1

II. Background 3

A. Thermoelectric Materials 3

1. Background 3

2. Thermopower 5

3. Electrical Conductivity 6

4. Thermal Conductivity 7

5. The Figure of Merit, ZT 8

B. Thermoelectric Generator Design Requirements 9

C. Thermoelectric Ceramics Material Development 10

III. Experimental Methods 12

A. Characterization Techniques 12

1. X-Ray Diffraction (XRD) 12

2. Density 13

3. Scanning Electron Microscopy (SEM) 13

4. BET 13

5. Coeffiecient of Thermal Expansion (CTE) 13

B. Thermoelectric Characterization 14

1. Thermoelectrical Measurement Systems 14

2. Electrical Conductivity Analyses 15

3. Seebeck Coefficient Analyses 16

4. Thermal Conductivity 17

5. Thermoelectric Generator Testing 19

IV. N-Type Thermoelectric $Ga_{3-x}In_{5+x}Sn_2O_{16}$ 21

A. Introduction and Background 21

B. Synthesis 24

1. Solid State Synthesis 24
2. Spark Plasma Sintering 24
C. Results and Discussion 25
1. XRD 25
2. Density 27
3. Scanning Electron Microscopy 28
4. Electrical Conductivity, Seebeck Coefficient, and Power Factor 30
5. Thermal Conductivity 36
6. Figure of Merit, ZT 38
V. P-type thermoelectric $Ca_3Co_4O_9$ 39
A. Background 39
B. Synthesis 42
C. Results and Discussion 43
1. XRD 43
2. Density 45
3. SEM 47
4. Electrical Conductivity, Seebeck Coefficient, and Power Factor 50
5. Thermal Conductivity 56
6. Figure of Merit, ZT 57
VI. Thermoelectric Generator Design and Analysis 59
A. TEG Design 59
B. Determining the Effectiveness of a Thermoelectric Generator 60
C. Fabrication Methods 61
D. Results and Discussion 62
1. CTE of Thermoelectric Legs 62
2. SEM of TEG Legs 62
3. Testing Results and Discussion 63
VII. Conclusions 66
VIII. Future Work 67
References 68

LIST OF TABLES

Page

Table I. Standard Uncertainties of Measurements Made by RIT Thermoelectric Generator Measurement System 20

Table II. Partial Occupancy of Cations of x=1: $Ga_2In_6Sn_2O_{16}$ 22

Table III. Density, % Porosity, % Theoretical Density 28

Table IV. Activation Energy of GITO Samples from 600°C-1000°C..... 34

Table V. Doping and Processing Scheme of $Ca_3Co_4O_9$ samples sintered at 900°C..... 42

Table VI. Doping and Processing Scheme of $Ca_3Co_4O_9$ Samples Sintered at 1100°C 43

Table VII. Density and BET Measurements of Ca-Co-O-based Materials Studied 46

Table VIII. Activation Energy of $Ca_{3-x}Sr_xCo_4O_9$ Samples 54

Table IX. Activation Energy of $Ca_{3-y}Ag_yCo_4O_9$ Samples 54

Table X. Linear Coefficient of Thermal Expansion for Materials Used in Thermoelectric Generators; For Each Material, N-type or P-type is Noted 62

Table XI. Parameters Measured for Thermoelectric Generator..... 63

Table XII. Calculated Values for Thermoelectric Generator..... 64

LIST OF FIGURES

Page

Figure 1. Schematic of a thermoelectric generator (TEG) as reported by Snyder et al. 4

Figure 2. Schematic of maximizing power factor of a semiconductor from Seebeck coefficient and electrical conductivity. 7

Figure 3. Processing flow chart for experimental methods. 12

Figure 4. Experimental sample set up for simultaneous measurement of dc electrical conductivity and Seebeck coefficient. 15

Figure 5. Illustration of linear regression used to determine Seebeck coefficient. 16

Figure 6. Seebeck coefficient analysis used in error analysis of the measurement 17

Figure 7. Schematic of the laser flash experiment set up. 18

Figure 8. Picture of RIT's TEG module test set-up. 19

Figure 9. Subsolidus phase diagram of the In_2O_3-Ga_2O_3-SnO_2 phase system at 1250°C. 21

Figure 10. C-axis view of anion-deficient fluorite structure of GITO 22

Figure 11. Schematic of spark plasma sintering set up. 25

Figure 12. XRD Pattern of GITO samples from 10° to 70° 2θ 26

Figure 13. Lattice parameters and unit cell volumes of GITO processed by pressureless sintering methods and spark plasma sintering. 27

Figure 14. Microstructural images of GITO samples produced by solid state synthesis, (a) x=0.6, (b) x=1.0, and (c) x=1.6. 29

Figure 15. Microstructural images of GITO samples consolidated by spark plasma sintering, (a) x=0.6, (b) x=1.0, and (c) x=1.6. 30

Figure 16. Direct electrical conductivity for GITO compositions and processes studied. Error bars are smaller than series symbols. 31

Figure 17. Direct electrical conductivity normalized to SPS theoretical density for GITO compositions and processes studied. 32

Figure 18. Seebeck coefficient as a function of temperature for GITO compositions and processes studied. 33

Figure 19. Seebeck coefficient as a function of temperature for GITO compositions and processes studied. 33

Figure 20. Power factor as a function of temperature. 35

Figure 21. Power factor of pressurelessly sintered samples normalized and compared to the SPS counter parts as a a function of temperature. 36

Figure 22. Thermal conductivity as a function of temperature. 37

Figure 23. Thermal conductivity normalized to percent theoretical density of SPS compositions as a function of temperature. 37

Figure 24. Figure of merit, ZT, as a function of temperature. 38

Figure 25. Schematic of the $Ca_3Co_4O_9$ crystal structure. 39

Figure 26. Phase diagram for CoO-cobalt system in air. 40

Figure 27. X-ray diffraction patterns of $Ca_{3-x}Sr_xCo_4O_9$ compositions sintered at 900°C. 44

Figure 28. X-ray diffraction patterns of $Ca_{3-x}Sr_xCo_4O_9$ compositions sintered at 1100°C. 44

Figure 29. X-ray diffraction patterns of $Ca_{3-y}Ag_yCo_4O_9$ compositions sintered at 900°C. 45

Figure 30. X-ray diffraction patterns of $Ca_{3-y}Ag_yCo_4O_9$ compositions sintered at 1100°C. 45

Figure 31. SEM images of $Ca_3Co_4O_9$ compositions sintered at 900°C 49

Figure 32. SEM images of $Ca_3Co_4O_9$ compositions sintered at 1100°C 50

Figure 33. Electrical conductivity results for $Ca_{3-x}Sr_xCo_4O_9$. 51

Figure 34. Electrical conductivity results for $Ca_{3-y}Ag_yCo_4O_9$. 52

Figure 35. Thermopower results for $Ca_{3-x}Sr_xCo_4O_9$. 53

Figure 36. Thermopower results for $Ca_{3-y}Ag_yCo_4O_9$. 53

Figure 37. Power factor results for $Ca_{3-x}Sr_xCo_4O_9$. 55

Figure 38. Power factor results for $Ca_{3-y}Ag_yCo_4O_9$. 55

Figure 39. Thermal conductivity results for $Ca_{3-x}Sr_xCo_4O_9$ 56

Figure 40. Thermal conductivity results for $Ca_{3-y}Ag_yCo_4O_9$. 57

Figure 41. Figure of Merit, ZT, results for $Ca_{3-x}Sr_xCo_4O_9$ 58

Figure 42. Figure of Merit, ZT, results for $Ca_{3-y}Ag_yCo_4O_9$. 58

Figure 43. Schematics of (a) unileg and (b) π-shaped thermoelectric modules..... 59

Figure 44. Photographs of TEG from a) bottom side view and b) top view with substrate removed..... 62

Figure 45. SEM images of (a) n-type and (b) p-type legs with silver paste. 63

ABSTRACT

Three thermoelectric compositional series, n-type $Ga_{3-x}In_{5+x}Sn_2O_{16}$, p-type $Ca_{3-x}Sr_xCo_4O_9$, and p-type $Ca_{3-y}Ag_yCo_4O_9$ were synthesized using solid state techniques. Comparisons of thermoelectric properties for $Ga_{3-x}In_{5+x}Sn_2O_{16}$ using pressureless sintering in air and spark plasma sintering consolidation were completed. Seebeck coefficient, electrical conductivity, and thermal conductivity were measured in argon from 200°C-1000°C. Seebeck coefficient was negative, indicating electron-type conduction. Overall electrical conductivity increased for SPS condensed samples. Figure of merit (ZT) of solid state sintered samples ranged from 0.23-0.46, and SPS condensed samples ranged from 0.08-1.12 at 1000°C. ZT values above 1.0 were observed due to increasing mobility and thermal conductivity values lower than 3W/m*K.

Comparisons of thermoelectric properties from different sintering temperatures were completed for $Ca_{3-x}Sr_xCo_4O_9$, and $Ca_{3-y}Ag_yCo_4O_9$. Seebeck coefficient, electrical conductivity, and thermal conductivity were measured in air from 200°C-800°C. Seebeck coefficient was positive, indicating hole-type conduction. Electrical conductivity increased as a function sintering temperature. Thermal conductivity of undoped samples increased from 0.5W/m*K to 1.5W/m*K at 800°C due to decreasing porosity, but did not decrease with doping due to secondary phases in the material. Doped compositions had ZT values ranging from 0.07-0.6, and undoped samples had ZT values ranging from 0.25-0.6 at 800°C. Similar ZT ranges are due to the wide range of electrical and thermal conductivity values observed.

Two compositions and processing methods were chosen, SPS consolidated $Ga_2In_6Sn_2O_{16}$ and $Ca_{3-x}Sr_xCo_4O_9$ sintered at 1100°C, for fabricating a simple oxide thermoelectric generator. A one leg pair π-module was fabricated and tested at two different hot side temperatures for ΔT of ~200°C, and ~600°C. Overall, electrical power generated was >1mW and efficiency was 0.21% when the hot side temperature was set at 800°C and cold side temperature was set at 200°C.

INTRODUCTION

The world's demands for energy are continually increasing, so to improve the sustainability of electricity the use of thermoelectric materials for waste heat applications is becoming more prominent in everyday life. Thermoelectric materials have the ability to produce an electric potential from a temperature differential, by using the Seebeck effect, and oxide materials are being investigated for their increased chemical and thermal stability. A thermoelectric generator (TEG) has the capabilities to use the resulting electrical potential and drive a current, thereby generating electricity directly from heat without any mechanical movement.

One of the main sources of waste heat is from industry; the U.S. industry sector has 20-50% of energy input being lost as waste heat. This percentage converts to about 6.4-16 quadrillion Btu of energy annually being wasted. Current technologies in the industry recover 1-3 quadrillion Btu/year, which leaves room for improvement in waste heat energy recovery as an avenue for power generation.[1]

High quality waste heat, temperatures above 650°C, allow for high-efficiency power generation, and are usually due to metal refining furnaces, glass melting furnaces, fume incinerators, and hydrogen plants. Usual methods of recovery are either using the waste heat for preheating air in other processes, or cooling the air to mid- or low-quality temperatures to be recovered by another recovery process. One of the main barriers that prevent recovery of high-quality waste heat is the increased corrosion that occurs at higher temperatures. Thermoelectrics can be an avenue to recover high-quality waste heat since at higher temperatures they can become more efficient by transforming more thermal energy into electrical energy. By using oxide materials, thermoelectrics would be able to be chemically stable to withstand the temperatures of high-quality waste heat. Oxide materials have adjustable electronic and phonon transport abilities, which allows for a wide range of properties, applications, and ultimately solutions for waste heat recovery. Finally, these materials have established synthesis and processing methods, which eliminates development time in the process of using these materials in industry. Thermoelectric oxides have a large potential to be effectively used in a niche area of

waste heat recovery in order to decrease the large amount of waste heat that is lost to the atmosphere; therefore being environmentally and economically beneficial.

Two groups of materials have been investigated: $Ga_3In_5Sn_2O_{16}$ and $Ca_3Co_4O_9$. These can be used as the n- and p-type thermoelectric materials needed to create a thermoelectric generator. Effects in thermoelectric properties will be determined via doping and different processing methods, and one composition of each material will be chosen for fabricating a thermoelectric generator. A simple thermoelectric generator will be tested to determine effectiveness between different temperature ranges that can be seen in industry. The goal of this work was to demonstrate an all oxide thermoelectric generator using $Ga_{3-x}In_{5+x}Sn_2O_{16}$ as the n-type material and $Ca_3Co_4O_9$ as the p-type material. Alfred University prepared and sintered GITO via pressureless and spark plasma sintering processes. A secondary objective was to determine the effect of SPS on the thermoelectric properties of the material. TAM Ceramics prepared powders and sintered samples of various compositions, which were characterized at Alfred University. Another secondary objective was to determine the properties of the materials prepared by TAM Ceramics. The simple thermoelectric generator was manufactured from these materials as a proof of concept that thermoelectric oxides have potential to be used by industry to decrease losses from waste heat.

This work has input from TAM Ceramics and Rochester Institute of Technology, as the research on p-type thermoelectric oxide $Ca_3Co_4O_9$ has originated from a New York State Energy Research and Development Authority (NYSERDA) grant. TAM Ceramics provided powder and parameters for $Ca_3Co_4O_9$ development, and RIT provided testing of the thermoelectric generator.

BACKGROUND

A. Thermoelectric Materials

1. Background

In 1820, Thomas Johann Seebeck discovered a phenomenon when he found that a compass needle would deflect when two dissimilar metals joined electrically in series were under a temperature gradient, which he called the *Seebeck effect*. Originally Seebeck called this *thermomagnetism*, but when Han Christian Oersted found connections between electricity and magnetism, with the actual reason for the phenomenon being the electrical current, the term *thermoelectricity* was coined.[2] Thermoelectricity is found not only in metals, but also in semiconductors and insulators.

Thermoelectric generators (TEGs) require p-type and n-type semiconductors aligned electrically in series and thermally in parallel, when a TEG is under a temperature gradient, the holes in the p-type and electrons in the n-type material diffuse to the cold side, thus creating a change in electric potential, as seen in Figure 1.[3] From the combination of electrical and thermal phenomena present in thermoelectric materials, TEGs can be used in waste heat applications to convert heat to electrical energy.

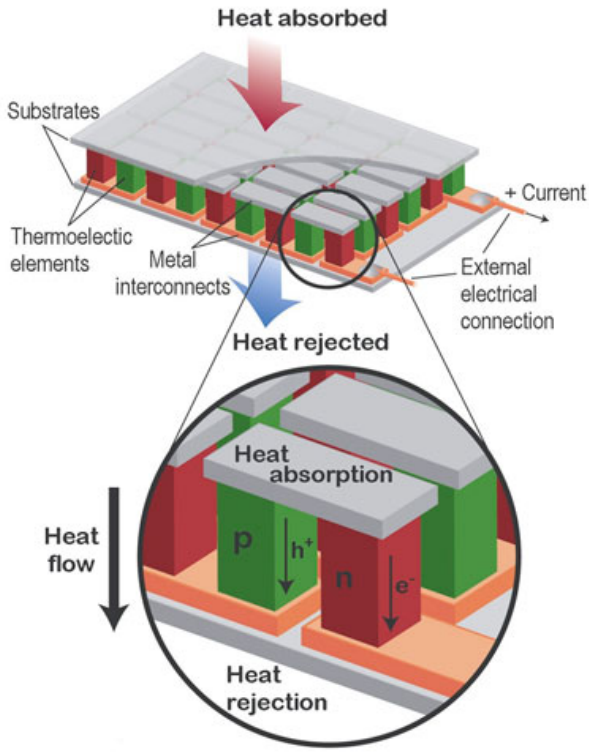

Figure 1. Schematic of a thermoelectric generator (TEG) as reported by Snyder et al.[2]

Thermoelectrics have been used in the past for power generation applications for aerospace and consumer applications. Successful thermoelectric generators are most commonly composed of bismuth telluride (Bi_2Te_3), lead telluride (PbTe), tellurides of antimony, germanium, and silver (TAGS), and silicon germanium (SiGe). Most of these materials are used specifically for radioisotope thermoelectric generators (RTGs) on space missions since the 1960's Cassini up through the recent Mars Curiosity rover.[4] Thermoelectrics are well suited for space applications because they have no moving parts, do not require maintenance, and have a long working life span.[5]

While thermoelectric generation has not had a major demonstration in the industrial sector, due to high capital costs, current advanced materials have the potential to achieve conversion efficiency over 15%. Since very few recovery techniques deal with high temperature waste heat, the 15% has the ability to be the main source of heat recovery into power generation for many industries such as metal refining and glass making. By using thermoelectrics for waste heat to electrical conversion, high power density (on the order of W/cm^3, W/kg) can be achieved, and thermoelectrics do not have

a lower heat limit to function, which allows a wide range of waste heat recovery temperatures.[6] The advantages of using this method are having the ability to recover waste heat, there are no emissions that are produced while in use, and it can be used on both portable and stationary devices (example: steam stacks and automobiles).

2. Thermopower

Thermopower, also known as the Seebeck coefficient, S or α, can be determined using Equation 1, where α is the Seebeck coefficient, V is voltage, and T is temperature.

$$\alpha = \frac{\Delta V}{\Delta T} \tag{1}$$

The Seebeck effect occurs due to an applied temperature gradient causes the charge carriers to diffuse from the hot side to the cold side, which creates a thermally induced current. The Seebeck coefficient can also be thought of as entropy per carrier as seen in Equation 2, where S is entropy, e is electron charge, Q is heat, k_B is Boltzmann's constant, and Ω are the number of configurations. To increase thermopower, an increase in entropy needs to occur, which usually occurs by maximizing spin orbital degeneracy in the electronic structure of the material so that the number of possible spin orbital configurations is at a maximum, thus maximizing configurational entropy.[7]

$$\alpha = \frac{\Delta S}{e} = \frac{Q}{eT} = \frac{k_B}{e}\ln(\Omega) \tag{2}$$

Metals were initially explored for Seebeck coefficients and were found to have thermopowers of tens of μV/K. Semiconductors were investigated and were found to have much higher thermopowers, on the order of a few hundred μV/K. Semiconductors can have either a positive or negative Seebeck coefficients. This is due to having different charge carriers, holes (p-type) or electrons (n-type), which will present a positive or negative Seebeck coefficient, respectively.[8]

3. Electrical Conductivity

Electrical conductivity, σ, is expressed in Equation 3,

$$\sigma = ne\mu \tag{3}$$

where n is carrier concentration, e is electron charge, and μ is the carrier mobility.
To achieve a high electrical conductivity both a high carrier concentration and high mobility are needed, which can be achieved by doping and thermal excitation. Temperature dependence on carrier concentration (n) can be seen in Equation 4,

$$n_i \propto T^{3/2} \exp\left(-\frac{E_g}{2k_B T}\right) \tag{4}$$

where E_g is the bandgap energy, and k_B is Boltzmann's constant.[9] In semiconductors, electron and hole mobilities are dependent on the impurity concentrations, temperature, and the ratio of minority to majority carriers.

Total thermopower also has a dependence on electrical conductivity if there is a large ratio of minority carriers in the material. As seen in Equation 5, if there is no extrinsic conduction through the addition of donor or acceptor sites, then the thermopower must be expressed as a weighted average of electrical conductivities. Crystal structure and bonding also affects the mobility of carriers in crystalline materials. Materials that have high degree of covalent bonding have higher mobilities, but unfortunately have higher thermal conductivities.[10]

$$S = \frac{S_n\sigma_n + S_p\sigma_p}{\sigma_n + \sigma_p} \tag{5}$$

To see an overview of the electrical properties for a given thermoelectric material, the power factor can be calculated from Equation 6, where PF is power factor, S is Seebeck coefficient, and σ is electrical conductivity. It is a commonly used way to determine if the material is a viable thermoelectric candidate without determining the

thermal conductivity of a material, since it incorporates the effect of increasing electrical conductivity can decrease thermopower. As seen in Figure 2[11], to maximize power factor, the carrier concentration should be on the order of 10^{20} carriers/cm^3.[12]

$$PF = S^2\sigma \tag{6}$$

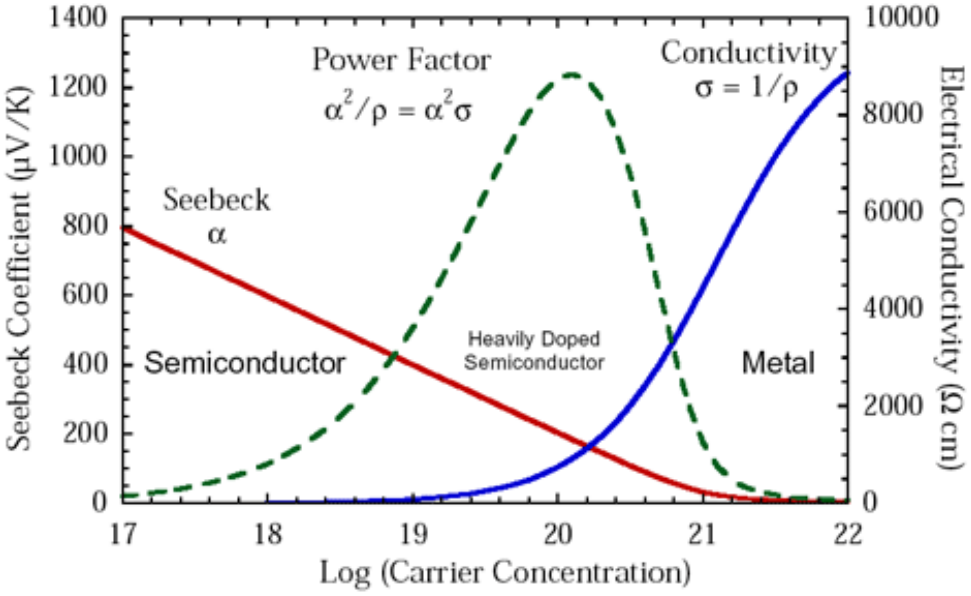

Figure 2. Schematic of maximizing power factor of a semiconductor from Seebeck coefficient and electrical conductivity.[11]

4. Thermal Conductivity

Thermal conductivity is related to heat transfer through a material either by electrons or phonons. Thermal conductivity (κ_T) can be broken into two parts: electrical thermal conductivity (κ_e) and lattice thermal conductivity (κ_L) as seen in Equations 7, 8, and 9,

$$\kappa_T = \kappa_E + \kappa_L \tag{7}$$

$$\kappa_E = L_o\sigma T \tag{8}$$

$$\kappa_L = \frac{1}{3}C\nu_s l_{ph} \tag{9}$$

where L_O is the Lorentz number, 2.45×10^{-8} V^2/K^2, σ is electrical conductivity, C is lattice specific heat, v_s is the speed of sound, and l_{ph} is the phonon mean free path. In oxides, κ_{ph} is often more pronounced than κ_e due to the material having lower concentrations of free electrons. To minimize κ_{ph}, and thus κ_T, phonon mean free path (l_{ph}) must decrease, as C and v_s are considered to be constant for a given material. There are three different ways to achieve this: adding phonon scattering centers into the lattice by adding point defects to the structure, such as adding heavier/rattling atoms; by creating materials with complex crystal structures such as phonon-glass electron-crystals (PGEC) that have regions in the structure that perform different functions that would allow high mobilities from the electron-crystal region and low thermal conductivities from the disordered phonon-glass region. The third way to decrease lattice thermal conductivity is by making multiphase composite nanostructures to scatter phonons and thus reduce the mean free path (l_{ph}) of the phonons.[13,14]

5. The Figure of Merit, ZT

For thermoelectric materials, no matter the type of carrier, the goal is to have a high figure of merit, Z or ZT, value as seen in Equation 10 and 11.

$$Z = \frac{S^2\sigma}{\kappa} = \frac{S^2}{\rho\kappa} \tag{10}$$

$$ZT = \frac{S^2\sigma T}{\kappa} = \frac{S^2 T}{\rho\kappa} \tag{11}$$

ZT is based on Seebeck coefficient S, electrical conductivity σ (or resistivity ρ), and thermal conductivity κ, with T being absolute temperature. Target values of thermoelectric oxides include: $\sigma > 10^3$ S/cm, $S > 150$ μV/K, $\kappa < 2$ W/mK, so that ZT>1 to compete with intermetallic thermoelectrics. While the above equations relate to an individual thermoelectric material, thermoelectric generators have a p-type and n-type material working as a couple, and both must be included in a new expression seen in Equation 12,

$$ZT = \frac{(S_p - S_n)^2 T}{(\rho_n \kappa_n)^{1/2} + (\rho_p \kappa_p)^{1/2}} \tag{12}$$

where the subscripts p and n indicate p-type and n-type, respectively. The above equations illustrate the need to have following requirements for thermoelectric materials: high electrical conductivity and Seebeck coefficient, and low thermal conductivity all in the same temperature range.

B. **Thermoelectric Generator Design Requirements**

The efficiency of a thermoelectric generator is given by Equation 13,

$$\eta = \left(\frac{T_H - T_C}{T_H}\right)\left(\frac{\sqrt{1+ZT}-1}{\sqrt{1+ZT}+\frac{T_C}{T_H}}\right) \tag{13}$$

where η is efficiency, T_C and T_H are the cold and hot temperatures, respectively, and ZT is the thermoelectric figure of merit. Efficient power generation requires significant temperature gradients and large ZT values are necessary.

In a practical device, other factors need to be considered such as strength and coefficient of thermal expansion (CTE). While TEGs have no mechanical movement, both compressive and shear strengths must be improved to combat potential damage to the materials during assembly and use, since mechanical and thermal shocks can occur. Matching the coefficient of thermal expansion of the p-type and n-type material is necessary to prevent extra stresses that can develop while the TEG is in use. A difference in CTE causes a proportional change in shear stress to thermal gradient due to the fractional change in the size of the legs. The larger the difference in CTE, the larger the stresses, which can then affect the contact interface the thermoelectric legs have with the substrate and decrease the lifetime and efficiency of the TEG.[15]

C. **Thermoelectric Ceramics Material Development**

Intermetallic thermoelectrics are the most commonly used materials in the thermoelectric field for their use in RTGs. These alloys possess the desirable ZT>1, but in application are not optimal at high temperatures due to decomposition, oxidation, and melting at high temperatures. Also these intermetallic materials, such as TAGS and BiTe, are heavy metals, and the toxicity raises safety concerns during synthesis and removal.[16]

Oxide thermoelectric materials have a greater chemical and thermal stability over their intermetallic counterparts, which can increase both the temperature and environmental range that these generators can operate in. Ceramic oxide thermoelectric materials are able to function at temperatures in the 600ºC-1200ºC ranges, which also allows for more heat energy to be converted into electrical energy. Unfortunately oxide materials have their disadvantages, which are hindering the progress of increasing the figure of merit value, ZT. Oxides inherently have a lower electrical conductivity from metallic conduction, lower Seebeck coefficient due to a lower voltage gradient, and have a higher thermal conductivity, all of which limits ZT in Equation 11. This can therefore be seen as decreasing the overall efficiency of the thermoelectric generator in Equation 13.

Progress has been made on improving thermoelectric oxides, with the main focus for p-types on cobalt-based oxides. Cobalt-based oxides, such as Na_xCoO_2, have what is called a misfit-layered structure, and have two types of unit "nanoblocks" in their structure containing two different compositions and symmetries, which allow for different electronic and phononic transports to function independently and allow high thermoelectric performance.[17] For Na_xCoO_2, the Na content x varies from 0.3-1.0 which changes the phases of Na_xCoO_2 to α, α', β, or γ. For thermoelectrics, the properties desired lie in the $0.55<x<0.7$ range, which is the γ phase, and was first synthesize in the 1970s, but not investigated for thermoelectrics until 1997, where a ZT value of 0.7 was observed for single crystals.[18,19] The crystal structure of Na_xCoO_2 has a CdI_2-type CoO_2 layer with a Na layer alternating in the c-axis. At room temperature this material has low resistivity (ρ=200μΩcm), high thermopower ($100<S<150\mu V/K$), and low thermal conductivity ($\kappa=5 Wm^{-1}K^{-1}$). The low resistivity is due to the conducting electrons in the CoO_2 layer, which are not effected by the disordered Na layer. Originally, κ was expected

to be much higher due to the lightness of the oxygen atom, but the lattice thermal conductivity of the cations in the CoO_2 layer allow for phonon scattering and decrease κ. While the thermopower is on the range of traditional thermoelectric semiconductors, the low-spin-state of Co^{4+} allowing for large entropy conflicts with the low-spin-state of Co^{3+} with zero entropy limits thermopower to ~154μV/K.[20] Overall polycrystalline Na_xCoO_2 can have ZT values upwards of 0.4, but due to the formation of the secondary phases at high temperature, Na_xCoO_2 is no longer an avenue for high temperature thermoelectrics. To decrease both resistivity and thermal conductivity, more complicated and more stable Co-based structures can be used, such as $Ca_3Co_4O_9$ or $Bi_2Sr_2Co_2O_y$.

Strontium titanate, $SrTiO_3$, has been explored in many different ways for n-type thermoelectric uses. Strontium titanate-based materials have many different avenues for changing the electron and heat transport properties, such as stoichiometry, crystallite orientation, and defects in grains and grain boundaries. Polycrystalline $SrTiO_3$ is common as an avenue for research into practical devices since it is both cost effective and has a low thermal conductivity, due to phonon scattering at grain boundaries. While the thermal conductivity of polycrystalline $SrTiO_3$ is smaller than its single crystal form, the power factor values are lower than obtained by single crystals. By using $SrTiO_3$ in the form of a Ruddleden-Popper phase $SrO(SrTiO_3)_n$, this natural supperlattice can decrease thermal conductivity further while keeping the electrical conductivity properties similar to $SrTiO_3$. Ruddleden-Popper materials have the formula $A_{n+1}B_nO_{3n+1}$, and is a hybrid structure with alternative layers of rock salt AO and perovskite ABO_3 structure that is represented as $AO(ABO_3)_n$. By using this family of materials the thermal conductivity decreases for $SrTiO_3$ (κ=7$Wm^{-1}K^{-1}$) as compared to $SrO(SrTiO_3)_1$ (κ=5$Wm^{-1}K^{-1}$) and even further with $SrO(SrTiO_3)_2$ (κ=3$Wm^{-1}K^{-1}$). This reduction in thermal conductivity is caused by decreasing the phonon mean free path from the increase in $SrO/SrTiO_3$ interfaces as *n* increases. By having the Ruddleden-Popper phase and through doping, this material has so far been found to have a ZT~0.25 at 1000K, as compared to the undoped phase reaching ZT~0.15 at 1000K.[21]

EXPERIMENTAL METHODS

The experimental methods can be summarized in Figure 3. Powders were synthesized and sintered for thermoelectric properties and materials characterization. From the sintered compacts, the thermoelectric generator was fabricated and characterized.

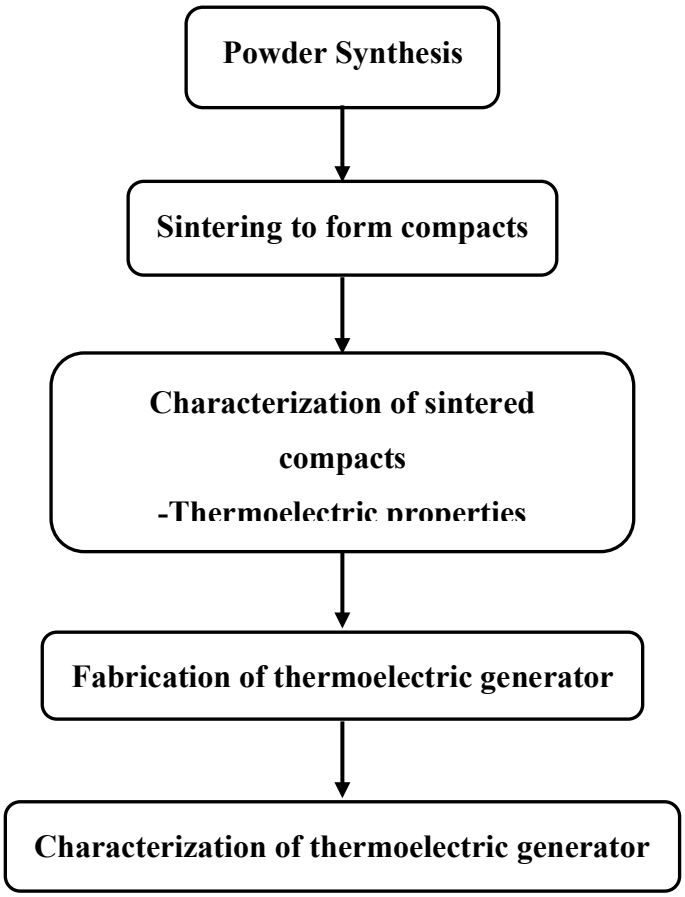

Figure 3. Processing flow chart for experimental methods.

A. Characterization Techniques

1. X-Ray Diffraction (XRD)

Product powders and compacts were analyzed by X-ray diffraction at room temperature using a Bruker D2 Phaser X-ray diffractometer equipped with Cu$K\alpha$ radiation (Bruker AXS, Germany). Data was collected from 10-70° 2θ with a step

size of 0.03° 2θ/second. DIFFRAC.EVA software (Bruker AXS, Germany) was used for phase analysis of diffraction patterns, and Jade 9 software (MDI, Inc, Livermore, CA) was used to determine lattice parameters of the unit cell.

2. Density

Density measurements were taken on sintered compacts. Archimedes method was used, and densities were determined using ASTM Standard C373-88 as a guideline.[22] Samples were dried for 3hr, and the dry mass (D) recorded. Then samples were put under a vacuum in de-ionized water for 12hr. After the 12hr period, the samples were weighed while suspended in water (S). The samples were then blotted with a damp kim-wipe and their saturated mass (M) was recorded. Bulk density (ρ) was found using Equation 14, % open porosity ($\%P$) was found using Equation 15.

$$\rho = \frac{D}{M - S} \times \rho_{H_2O} \tag{14}$$

$$\%P = \frac{M - D}{M - D} \times \rho_{H_2O} \times 100\% \tag{15}$$

3. Scanning Electron Microscopy (SEM)

Microstructural images were taken with a Quanta 200f environmental electron microscope (FEI, Boston, MA) using fractured surfaces. Scanning electron, backscattered election, and backscattered scanning electron images were taken using 20.0kV and a spot size of 3.0μm. Fractured surfaces were gold coated before imaging.

4. BET

Surface areas of calcined powders were analyzed using a Tristar 3000 V6.07 Analyzer (Mircomeretics, Norcross, GA). Samples were degassed with helium gas for one hour, and measurements were taken using nitrogen gas.

5. Coeffiecient of Thermal Expansion (CTE)

Linear thermal expansion was determined using a NETZSCH DIL 402 PC (NETZSCH Group, Germany). Samples were cut into bars with 10-11mm lengths and

tested in helium from room temperature up to 800°C or 1000°C. Linear thermal expansion was calculated using Equation 16.

$$\alpha_L = \frac{1}{L_0}\left(\frac{dL}{dT}\right) \tag{16}$$

B. Thermoelectric Characterization

Thermoelectric characterization is completed by two separate measurements to determine the electrical and thermal properties. Electrical measurements determine electrical conductivity and thermopower, and thermal measurements determine thermal conductivity.

1. Thermoelectrical Measurement Systems

Direct current electrical and absolute thermopower measurements were made simultaneously to determine electrical conductivity and Seebeck coefficient (absolute thermopower). Sintered compacts were cut into ~4x4x12mm bars for electrical and thermopower characterization. Samples were polished and then notched at the 1/4 and 3/4 length marks. Samples were then painted with gold paste on the ends and along the notches on the sample. Gold wire was wrapped around the notched points on the sample.

N-type thermoelectric measurements were preformed using an in-house computer controlled system that includes a current source (Model 2700 Keithley Instruments, Inc, U.S.A.) and a digital multi-meter (Model 2400 Keithley Instruments, Inc, U.S.A.) based on the 4-point steady state gradient technique as shown in Figure 4.[23] Samples were placed off-center in a tube furnace to create a temperature gradient of ~20K along the length of the sample. Four S type thermocouples (Pt/Pt-13%Rh) were attached to the notched and painted sample by aligning two gold foil pieces at the bar ends, and wrapping the two inner thermocouples to the gold wires that were wrapped on the notched points on the sample. Samples were purged of air and back-filled with argon gas. Percentage of oxygen was also measured using an oxygen analyzer (Series ZR800 Illinois Instruments, Johnsburgh, IL) for samples tested in argon.

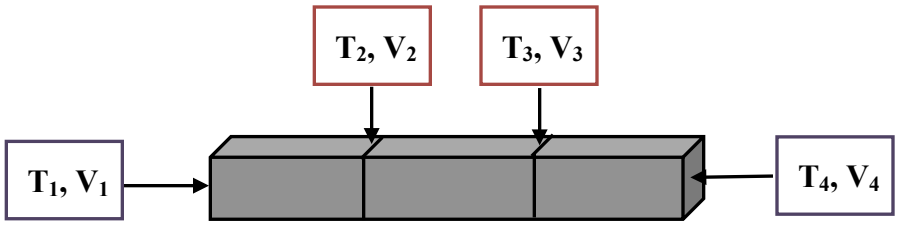

Figure 4. Experimental sample set up for simultaneous measurement of dc electrical conductivity and Seebeck coefficient.

P-type thermoelectric measurements were made in an in-house computer controlled system that includes a current source (Model 2700 Keithley Instruments, Inc, U.S.A.) and a digital multi-meter (Model 2400 Keithley Instruments, Inc, U.S.A.) based on the 4-point steady state gradient technique as shown in Figure 4. Three samples were measured simultaneously in air with the bar samples resting on top of the four thermocouples and a vertical alumina push rod on top of the sample to hold the bar in place.

For both systems, thermal equilibration was obtained by holding the furnace at each temperature measured for 60min before measurements were taken. Raw data was obtained by the computer-controlled equipment using the 4-point measurement technique via LabView. Temperature difference was recorded between all points (ΔT at 1-2, 1-3, 1-4, 2-4, 2-3, 3-4), followed by reading the six electrical potential measurements (ΔV at 1-2, 1-3, 1-4, 2-4, 2-3, 3-4). Then the forward resistance was found using a current of 20mA in the forward direction between points 1-4, and the voltage drop between 3-2 was measured. The reverse resistance was found by applying 20mA in the reverse direction between points 4-1, and the voltage drop between 2-3 was measured. Data was manually reviewed and outlier points were removed.

2. Electrical Conductivity Analyses

Electrical conductivity was determined from the measured forward and reverse resistances measured. Electrical conductivity was calculated from Equation 17,

$$\sigma = \frac{l}{R_{avg} A} \tag{17}$$

where σ is electrical conductivity, R_{avg} is the average of the forward and reverse resistance, l is the length between points 1 and 4 along the bar (Figure 4), and A is the cross-sectional area of the bar. Electrical conductivity values reported are the average of five measurements, have a standard deviation of <1% of the averages, and reported in units of S/cm.

3. Seebeck Coefficient Analyses

Seebeck coefficient was determined by using a linear regression of a ΔV vs. ΔT plot as shown in Figure 5, which was made from the data produced from five individual readings. The slope obtained was corrected from the use of platinum thermocouples according to $\alpha_{measured} = \alpha_{sample} + \alpha_{Pt}$, where α_{Pt} is determined using Equation 18, and reported in units of μV/K.[24]

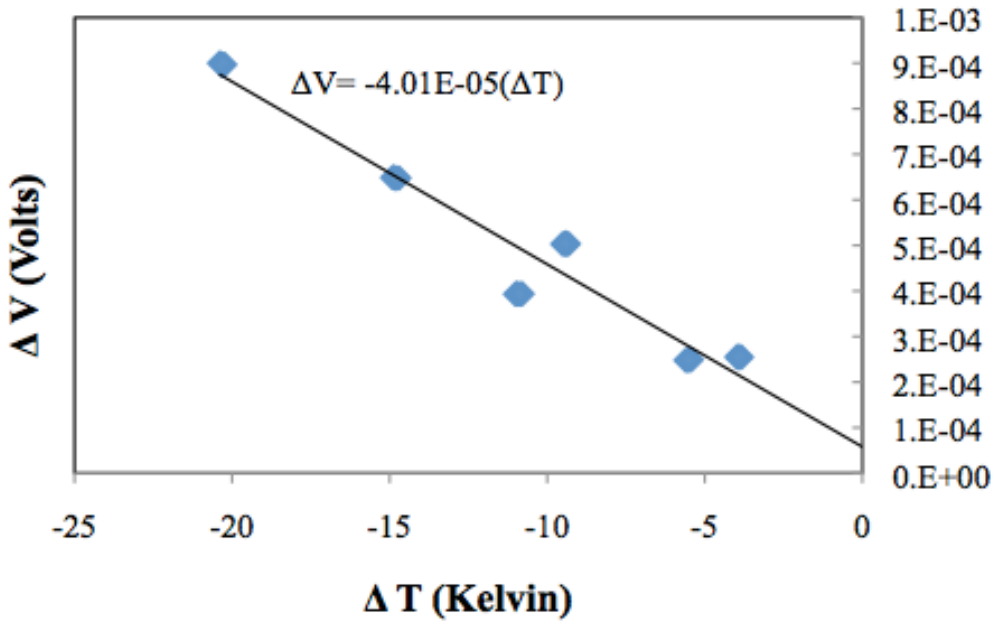

Figure 5. Illustration of linear regression used to determine Seebeck coefficient.

$$\alpha_{Pt} = 0.186T\left[\exp\left(-\frac{T}{88}\right) - 0.0786 + \frac{0.43}{1+\left(\frac{T}{84.3}\right)^4}\right] - 2.57 \quad (18)$$

Error analysis of Seebeck coefficient was determined by incorporating a zero intercept into the linear regression, as it would create an ideal ΔV vs. ΔT plot. Error in the measurements can be estimated by the difference in the slope of the linear regression and the slope of the linear regression with the zero intercept. The illustration of the error estimation can be seen in Figure 6. Seebeck coefficient error calculated is <10% of reported values for T<300°C and <5% of reported valued for T>300°C.

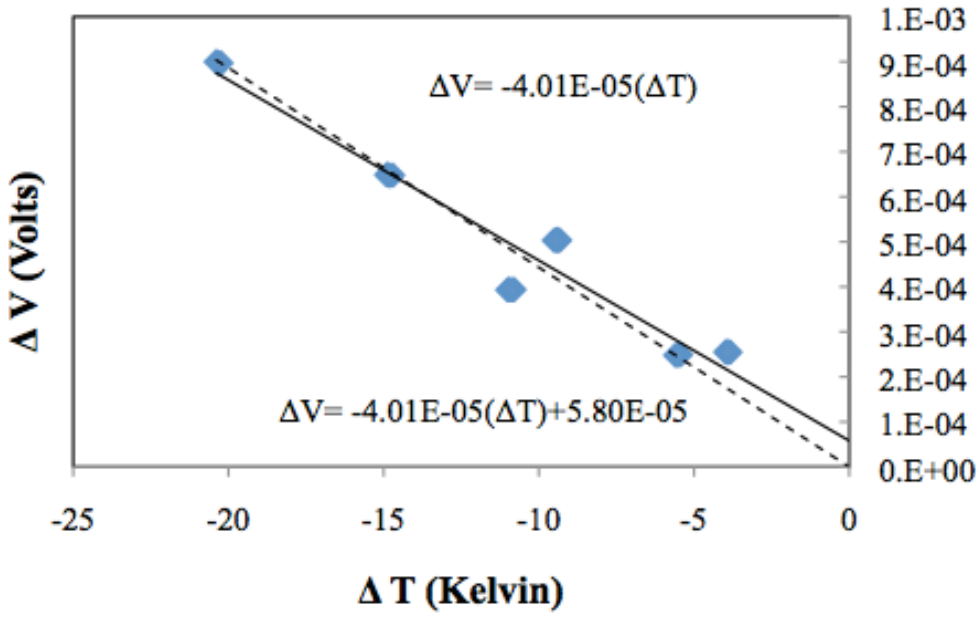

Figure 6. Seebeck coefficient analysis used in error analysis of the measurement. Dashed line results from deviation from due to driving the intercept to zero.

4. Thermal Conductivity

Thermal conductivity was calculated from Equation 19, where κ is thermal conductivity, ρ is geometrical density, C_p is specific heat, and D_{th} is thermal diffusivity.

$$\kappa = \rho C_p D_{th} \tag{19}$$

The laser flash method is used to determine C_p and D_{th} of bulk samples at elevated temperatures.[25] Both thermal diffusivity and specific heat were determined simultaneously using a DLF-1200 laser-flash thermal diffusivity system (TA Instruments, New Castle, DE). Samples were core drilled to 1/2" sized disks with thicknesses ranging from 1-3mm, which were polished, and coated with graphite spray immediately before testing to create identical surface characteristics. An infrared opaque sample at thermal equilibrium is hit with a high intensity laser pulse at the front face of the sample for a short period of time, see Figure 7. An IR detector observes the back face, so that temperature change with time can be produced as a thermogram. The thermogram produced is used to determine the time when the sample reaches half of the maximum temperature ($t_{1/2}$) over the length of the sample (L), so that thermal diffusivity can be calculated in Equation 20.

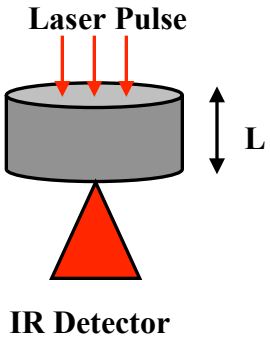

Figure 7. Schematic of the laser flash experiment set up.

$$D_{th} = 0.138786 \frac{L^2}{t_{1/2}} \tag{20}$$

Specific heat is measured by using a comparative method to a known reference standard, and creating a ratio of the maximum temperature rise of each sample measured during the experiment.[26] Thermographite and molybdenum references were used to for specific heat measurements.

5. Thermoelectric Generator Testing

Thermoelectric generator testing was completed at the Rochester Institute of Technology in Rochester, NY. The in-house testing set-up, seen in Figure 8, uses a guard heater arrangement to accurately measure heating rates, and decreases heating losses. The heater blocks used are comprised of a copper core with nickel electroplating. A plate is arranged to hold TEGs with a $10mm^2$ substrate surface area. Hot side measurements can be tested up to 800°C, and cold side measurements can be tested from 500°C down to 50°C. The hot and cold side temperatures were measured with type-K thermocouple using a NI 9213 (National Instruments, USA). By using a Kikusul PLZ4W programmable electronic load, a true short circuit can be measured. The TEG is clamped down in the system by using a piston, which can also vary the pressure put on the entire module during testing. Measurements that can be taken are overall electrical resistance, overall TEG Seebeck coefficient, thermal conductance, power generated, current, and TEG efficiency. Each measurement recorded is the average of 50 samples at 100Hz. Measurements are taken in an argon atmosphere.

Figure 8. Picture of RIT's TEG module test set-up.

This arrangement measures the following: module hot side temperature (T_H), module cold side temperature (T_c), open circuit voltage (V_o), short circuit voltage (V_s), heat rate into the hot side of the module (q), and short circuit current (I_s). Equations 21, 22, and 23 are used to determine thermopower of the TEG, resistance of the TEG, and thermal conductance of the TEG, respectively. The open circuit current (I_o) is assumed to be zero for Equation 22.

$$\alpha_{TEG} = \frac{V_O}{\Delta T} = \frac{V_O}{T_H - T_C} \tag{21}$$

$$R_{TEG} = \frac{V_O - V_S}{I_O - I_S} \tag{22}$$

$$\mathrm{K}_{TEG} = \frac{q}{\Delta T_O} \tag{23}$$

By taking length measurements (l) of the thermoelectric legs and the TEG, Equations 24 and 25 can be used to determine electrical conductivity and thermal conductivity of the module.

$$\sigma_{TEG} = \frac{R_{TEG}}{l} \tag{24}$$

$$\kappa_{TEG} = \frac{\mathrm{K}}{l} \tag{25}$$

Standard uncertainties for this instrument are identified in Table I.

Table I. Standard Uncertainties of Measurements Made by RIT Thermoelectric Generator Measurement System

Measurement	T_H	T_C	Q	V_o	I_S	V_S
Uncertainty	0.5°C	0.5°C	1.0W	0.001mV	0.01mA	0.1mV

N-TYPE THERMOELECTRIC $GA_{3-X}IN_{5+X}SN_2O_{16}$

A. Introduction and Background

$Ga_{3-x}In_{5+x}Sn_2O_{16}$, now referred to as GITO, is the n-type semiconducting oxide that is being investigated in this work. GITO was identified initially as a transparent conducting oxide (TCO) in 1997 by Edwards *et al*. as a method to produce TCO's with decreasing In content while keeping a similar crystal structure to the commonly used material In_2O_3. Good TCO's (>1000S/cm electrical conductivity and >80% transmission of visible light as a thin film) are of interest for commercial applications such as photovoltaic cells, electrochromics, and flat panel displays. GITO is located in the T-phase of the subsolidus In_2O_3, Ga_2O_3, and SnO_2 ternary phase diagram in Figure 9. This phase occurs with constant Sn content, [Sn]=0.20, and [In] content from 0.52 to 0.66 on a cation basis thus expressed as $Ga_{3-x}In_{5+x}Sn_2O_{16}$, with x ranging from $0.3 \leq x \leq 1.6$.

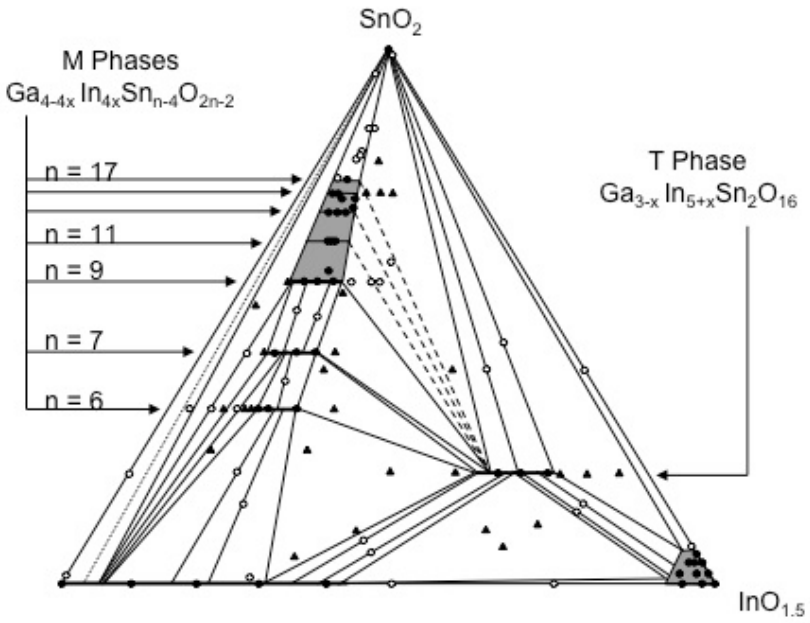

Figure 9. Subsolidus phase diagram of the In_2O_3-Ga_2O_3-SnO_2 phase system at 1250°C. Solid circles are single-phase compositions, open circles are two-phase compositions, and triangles are three-phase compositions.[27]

GITO has a tetragonal anion-deficient fluorite structure (space group $I4_1/a$), similar to the In_2O_3 bixbyte structure. The anion-deficient fluorite structure is derived

from a cubic-fluorite parent structure by a 26.6° rotation about the *c*-axis and removal of 1/5 of the anions, in this case oxygen. Also, the cations (Ga, In, Sn) are shifted away from the formal vacancies of the parent structure, while the anions (O) are shifted toward the formal vacancies of the parent structure. The anion-deficient fluorite structure, as seen in Figure 10, shows three different cations with 4-fold, 6-fold, 7-fold, and 8-fold coordination with the oxygen anion. Table II shows the partial occupancy of cation sites for x=1 composition ($Ga_2In_6Sn_2O_{16}$), which indicate different cations on the MO_6 and MO_7 coordination sites. Sn content does not change in this phase, which indicates that Sn serves as structural component in the structure, and In serves as a dopant on the Ga sites.

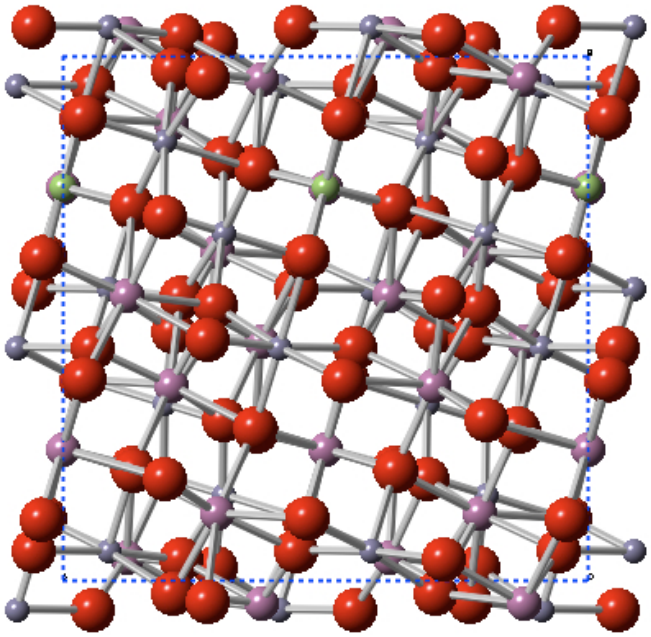

Figure 10. C-axis view of anion-deficient fluorite structure of GITO

Table II. Partial Occupancy of Cations of x=1: $Ga_2In_6Sn_2O_{16}$

Coordination Geometry of Cation	Ga occupancy (%)	In occupancy (%)	Sn occupancy (%)
4-Fold	100	0	0
6-Fold	25	33	42
7-Fold	0	92	8
8-Fold	0	100	0

GITO ranges in color from yellow-green (low In content) to green (high In content), and has an optical band gap of ~3eV. Conductivity values of 375S/cm have been reported for bulk GITO, and recent work has been done on the role on the In/Ga ratio for electrical properties.[28] [29] The conductivity of GITO can be attributed to the In^{3+} cations in the *5s* conduction band, since when undoped by In, the *5s* band remains empty and is a poor semiconductor.[30] Increasing the conductivity of GITO is possible due to the formation of oxygen vacancies through Equation 26 through reduction after forming GITO.[31]

$$O_O^x \rightarrow \frac{1}{2}O_2(g) + V_o^{\bullet\bullet} + 2e^- \tag{26}$$

Conductivities as high as 1888S/cm have been recorded by doping with In, and annealing GITO in forming gas at 500°C.[32]

While GITO has a tenfold lower electrical conductivity than Sn-doped In_2O_3, it has less [In] and therefore an economical advantage over In_2O_3. Attempts to dope GITO with another cation, such as Sn, have negligible improvements due to the limit of Sn solubility in the structure past the stoichiometric 20% cation basis. Thermal conductivity is quite low due to an octahedra site of the cations where the M cations (Ga=25%, In=33%, and Sn=44%) are distributed randomly thus causing a decrease in the mean free path of the phonons (l_{ph}). The lower thermal conductivity can also be attributed to the large mass difference between Ga^{3+} as compared to In^{3+} and Sn^{4+}.

For thermoelectrics, Ge-doped In_2O_3 has been observed to produce a ZT value of 0.45 at 1273K, but has much higher In content as compared to GITO, which was reported by *Bhame et al.* to have a ZT value of 0.23 at 1000K using solid state sintering methods. The semimetallic behavior of GITO can be attributed to the In^{3+} cation, since increasing [In] causes an increase in electrical conductivity with a decrease in the absolute Seebeck coefficient due to the increase in carrier concentration, and thermal conductivity increases due to the decrease in randomness of the MO_6 octahedra when In replaces Ga in the structure.[33]

In this work, GITO thermoelectric properties are investigated using two different processing methods: pressureless sintering and spark plasma sintering. Spark plasma

sintering is investigated as a processing avenue to improve thermoelectric properties of GITO, as it has not been investigated in the past, and will be compared to pressureless sintering tested at Alfred University and in current literature. Also GITO will be investigated in order to determine a composition and sintering method in order to be incorporated into a thermoelectric generator for the first time.

B. Synthesis

1. Solid State Synthesis and Presureless Sintering

Samples of $Ga_{3-x}In_{5+x}Sn_2O_{16}$ (x=0.6, 1.0, 1.6) were prepared using solid state synthesis techniques. Stoichiometric amounts of In_2O_3 (Sigma Aldrich ≥99.99%), Ga_2O_3 (Sigma Aldrich ≥99.99%), and SnO_2 (Sigma Aldrich ≥99.99%) were ground together using mortar and pestle. Pellets were pressed together with 5% PVA binder solution, and heated in high-density alumina crucibles at 1250°C for 72hrs and quenched in air. The pellets were placed on a powder bed of the same composition during firing in order to prevent contamination from the alumina crucibles.

2. Spark Plasma Sintering

Spark plasma sintering (SPS) is a processing technique that allows for high heating rates, and creates high-density materials. Uniaxial pressure and current are applied to provide rapid Joule heating and sintering of materials. GITO powders were made using the same method as described above. Resulting powder was placed in a graphite die, as seen in Figure 11, and heated at a rate of 100°C/min and consolidated with 14kN of force at 850°C for 30min.

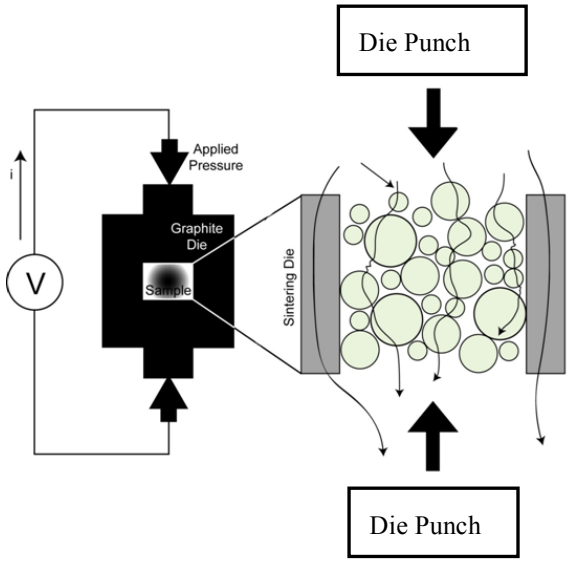

Figure 11. Schematic of spark plasma sintering set up.

C. Results and Discussion

1. XRD

Figure 12 shows the X-ray diffraction patterns of both the pressureless (CS) and spark plasma (SPS) sintered samples. Sample patterns show phase purity based on PDF card #04-011-6302. For the x=1.6 pressureless sintered sample, there is a pronounced 344 peak at ~41° 2θ; it is not known why this peak is pronounced, but it is an allowable peak for the GITO structure.

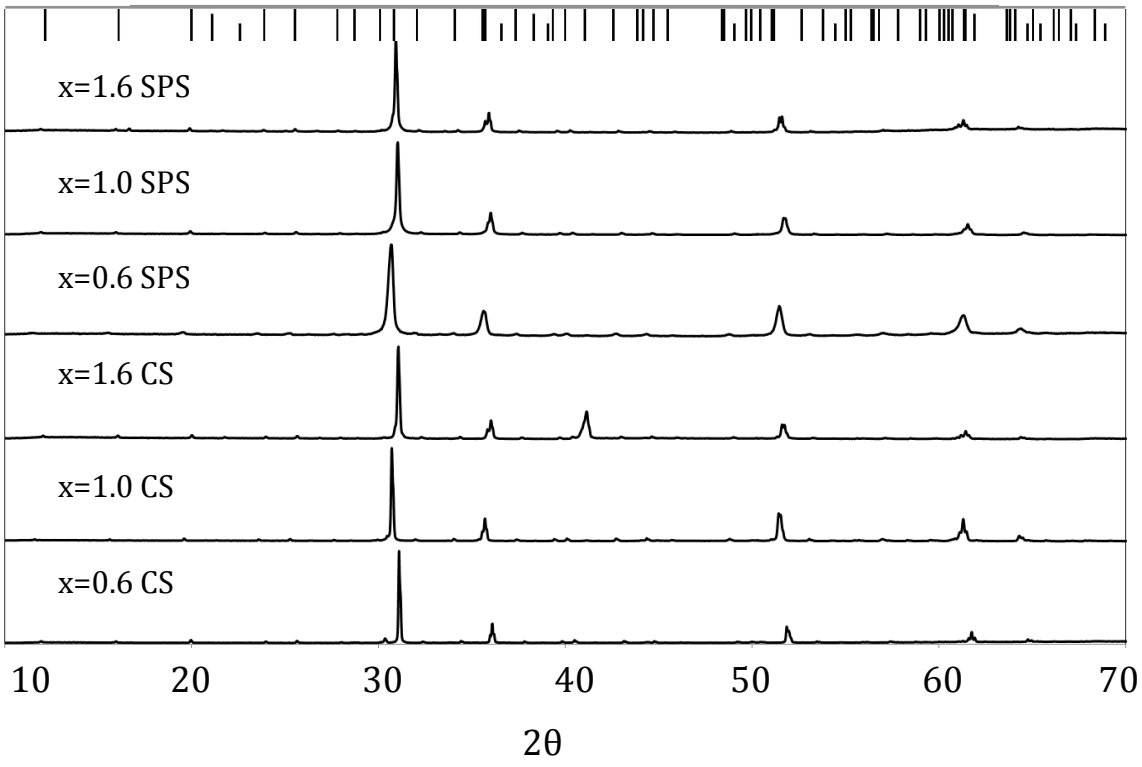

Figure 12. XRD Pattern of GITO samples from 10° to 70° 2θ.

Cell refinement of the GITO samples can be seen in Figure 13. The unit cell is increasing with increasing In content in both the a- and c-direction, and the SPS consolidated samples have smaller c-and a- lattice parameters except for the x=1.0 sample. The increase in axes lengths is due to the increase in size of ions from Ga^{3+} (47pm) to In^{3+} (62pm).

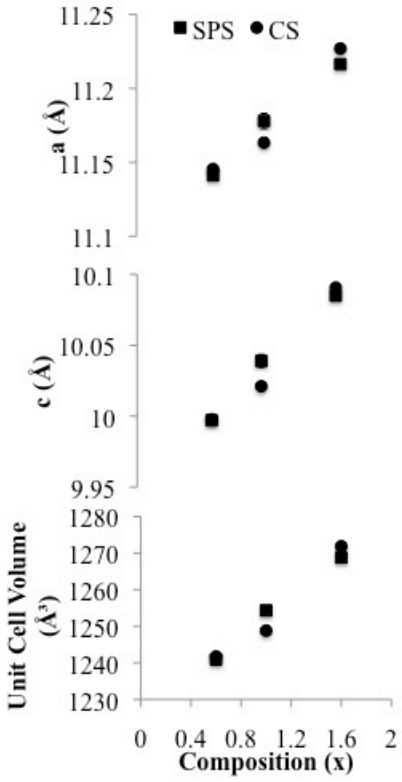

Figure 13. Lattice parameters and unit cell volumes of GITO processed by pressureless sintering methods and spark plasma sintering.

2. Density

Processing parameters and percentage of theoretical densities are compiled in Table III. Densities of sintered compacts were determined using the Archimedes method as mentioned earlier. Overall the theoretical densities should be increasing as indium content increases. The measured densities have an interesting trend occurring, since the percentage theoretical density does not seem to increase or decrease as a function of composition, but the x=1.0 samples are less dense than the x=0.6 and x=1.6 samples. When comparing the pressureless sintered (CS) samples to the SPS consolidated samples (SPS), the SPS consolidated samples have much higher percent of theoretical density, >96%, as the solid state synthesized samples at 50%<ρ_{Th}<61%. This dramatic increase in theoretical density in SPS consolidated samples is due to both the uniaxial pressure and application of high temperature during the SPS process. Pressureless sintered samples have percent theoretical densities similar to previously reported by *Edwards et al.* at 60-

65%, but dissimilar to *Bhame et al.* at 95%. Differences can be somewhat attributed to uniaxial pressing pressures before sintering: *Edwards et al.* pressed at 150MPa, *Bhame et al.* at 300MPa, and this work at ~4MPa.

Table III. Density, % Porosity, % Theoretical Density

Method	X	Composition	ρ_{Th}	Density	% Open Porosity	ρ_{Th} %
CS	x=0.6	$Ga_{2.4}In_{5.6}Sn_2O_{16}$	6.962	4.23	38.2	60.5
CS	x=1.0	$Ga_{2.0}In_{6.0}Sn_2O_{16}$	6.995	3.60	46.3	51.4
CS	x=1.6	$Ga_{1.4}In_{6.6}Sn_2O_{16}$	7.052	4.21	39.2	60.2
SPS	x=0.6	$Ga_{2.4}In_{5.6}Sn_2O_{16}$	6.962	6.82	0.40	97.5
SPS	x=1.0	$Ga_{2.0}In_{6.0}Sn_2O_{16}$	6.995	6.76	0.48	96.5
SPS	x=1.6	$Ga_{1.4}In_{6.6}Sn_2O_{16}$	7.052	6.83	0.39	97.5

3. Scanning Electron Microscopy

Microstructural images of fractured surfaces were taken with a scanning electron microscope. Images of each composition were taken of both solid state synthesized and SPS processed, and can be seen in Figure 14 and Figure 15, respectively. For each process there is little grain structure change as [In] content increases, but comparing the solid state sintered samples to the consolidated SPS samples there is a dramatic change in grain structure. The pressureless sintered samples have rounded grains on the order of ~1-5μm. This microstructure contains many interconnected, but open sections; this indicates a lower level of densification. The larger grains can be attributed to grain growth and coarsening due to the extended dwell timed during sintering. The SPS samples have more angular grains on the order of ~1-3μm. The grains are more ordered and packed with less pores between the grains, which indicates an overall higher density. This is due to the lack to grain coarsening during the SPS process due to the significantly shorter dwell time. The ordered grains can also be attributed to the uniaxial pressure on the sample during the SPS process. These SEM images generally confirm the density changes noted previously.

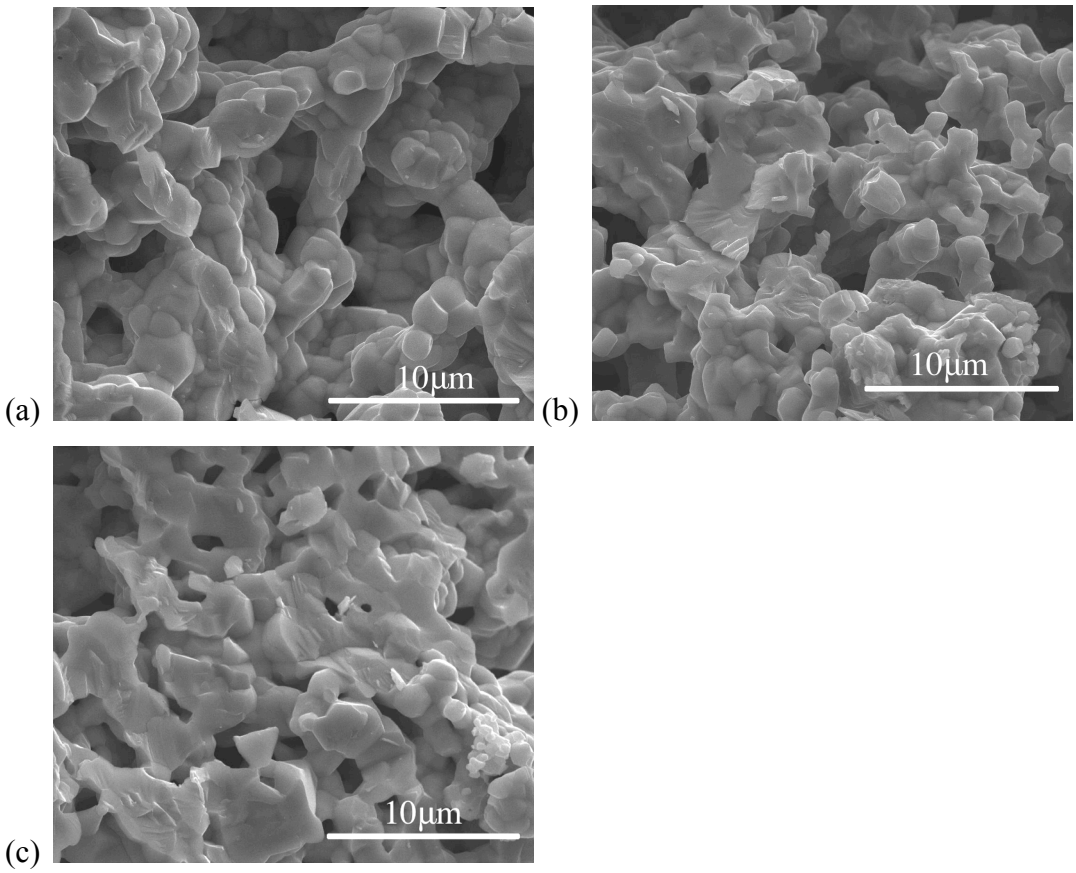

Figure 14. Microstructural images of GITO samples produced by pressureless synthesis, (a) x=0.6, (b) x=1.0, and (c) x=1.6.

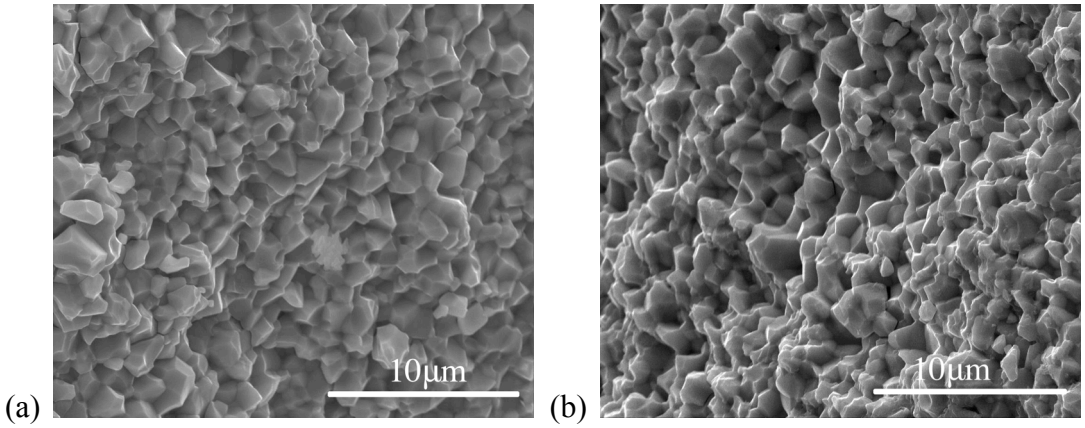

(c) 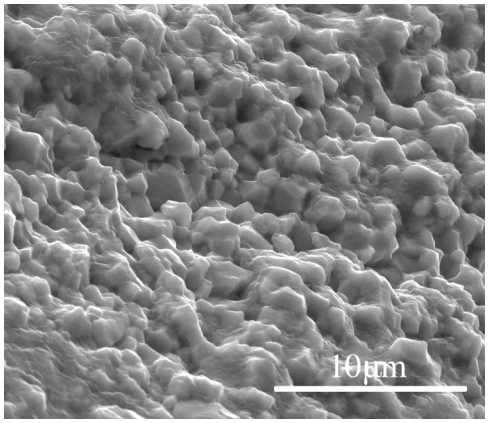

Figure 15. Microstructural images of GITO samples consolidated by spark plasma sintering, (a) x=0.6, (b) x=1.0, and (c) x=1.6.

4. Electrical Conductivity, Seebeck Coefficient, and Power Factor

Direct current electrical conductivity (σ) was measured from 200-1000°C for all GITO samples and are shown in Figure 16. Electrical conductivity is seen to decrease slightly with increased temperature until ~600°C and then increase as temperature increases. The increase in conductivity between processing methods can be attributed to two factors: the increase in density by using SPS, and the slight reduction of the material due to condensing in an inert atmosphere as opposed to air. By normalizing conductivity to the percent of theoretical density ($\%\rho_{Th}$) of the SPS samples, Figure 17 can be created. While the highest In-doped sample (CS x=1.6) does then have conductivities similar to its spark plasma sintered counterparts, the lower In-doped solid state synthesized samples have marginal increases in conductivity when normalized to density. The reduction of the material via SPS is a common phenomenon, and it can also be identified by the color change of the samples. The solid state synthesized samples are a green color; while the SPS consolidated samples are a grey color. Samples consolidated using SPS (SPS) have higher conductivities than their pressureless sintered (CS) counterparts. In general, the CS samples have minimal change after 600°C, which can mean either the carrier concentration or mobility is decreasing. CS x=1.6 has notably higher electrical conductivity than the other compositions. Bhame observed this trend as a "metallic like behavior", so the effects may most likely be attributed to a decrease in mobility. Also the magnitude of electrical conductivity is similar to that observed by Bhame.[34]

SPS samples have decreasing trends then increasing after approximately 600°C, and there is a systematic increase as x increases. After normalizing the SPS samples to percent theoretical density the SPS have higher electrical conductivities. This implies higher carrier concentration or higher mobility. Both could be plausible for the SPS samples: an increase in carrier concentration due to the creation of oxygen vacancies, and a decrease in mobility due to limiting mobility from grain boundaries.

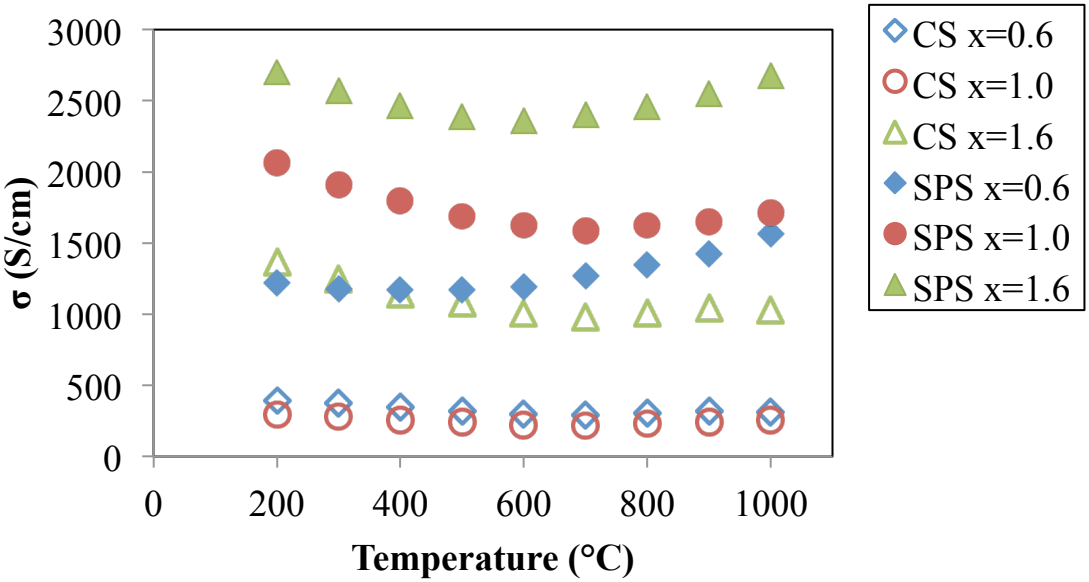

Figure 16. Direct electrical conductivity for GITO compositions and processes studied. Error bars are smaller than series symbols.

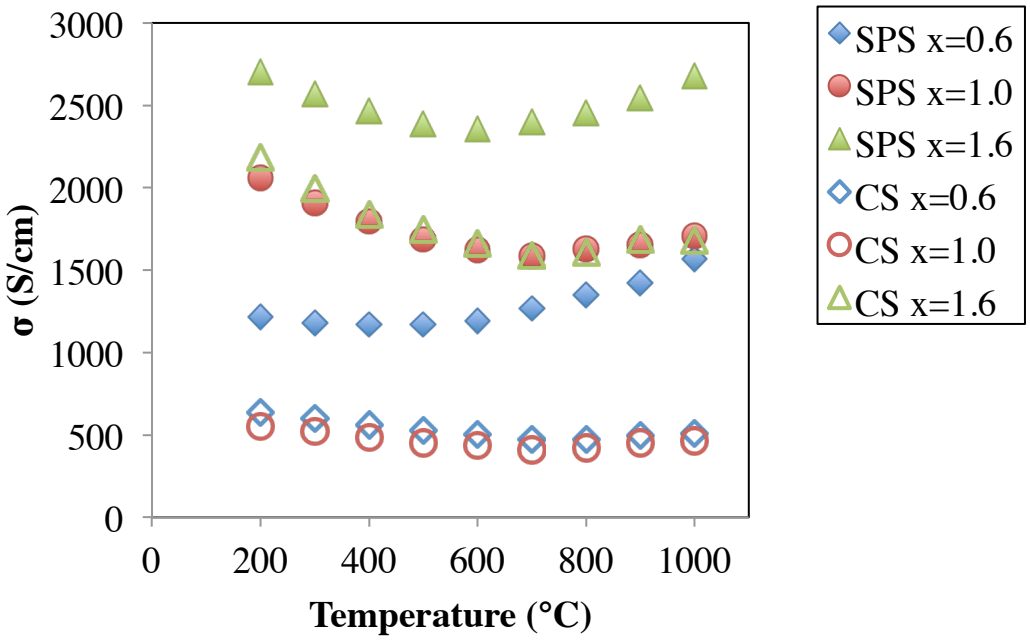

Figure 17. Direct electrical conductivity normalized to SPS theoretical density for GITO compositions and processes studied. Error bars are smaller than series symbols.

Thermopower was measured from 200-1000°C, and can be seen in Figure 18 and Figure 19. The Seebeck coefficient is negative, which indicates electrons are the majority carriers in the system. Seebeck coefficient becomes more negative with increasing temperature. Bhame *et al.* also observed this trend, but did not give possible explanations for this effect. This change in Seebeck implies decreasing carrier concentration, or an increase in mobility. For pressureless sintered samples, the Seebeck magnitude decreases as x increases, which indicates a carrier concentration increase with x and is expected. When compared to Bhame *et al.* the Seebeck coefficients are lower than what he observed at 1000K (727°C), but are similar in compositional and magnitude trends. For SPS samples, Seebeck is similar values for x=0.6 and x=1.6, but the 1.0 is considerably lower, and are not sure why, so SPS x=1.0 will require further investigation. For SPS x=0.6 and x=1.0 samples, Seebeck coefficient has decreasing magnitude which is due to an increase in carrier concentration and consistent with electrical mobility.[35]

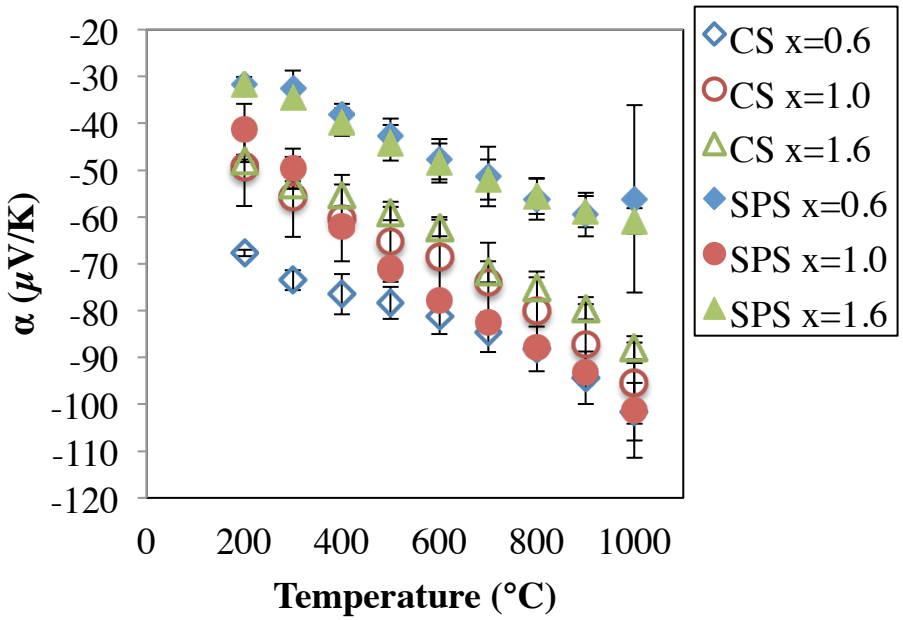

Figure 18. Seebeck coefficient as a function of temperature for GITO compositions and processes studied.

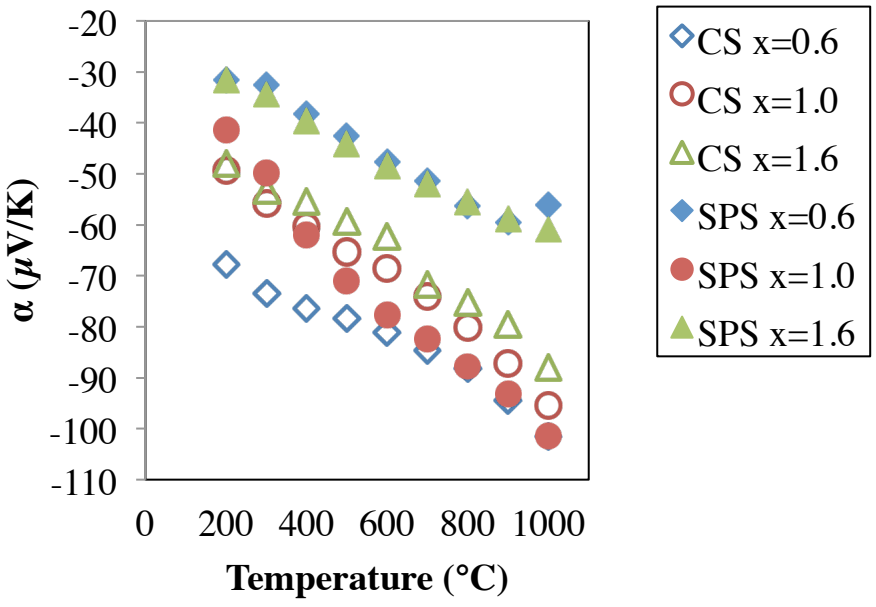

Figure 19. Seebeck coefficient as a function of temperature for GITO compositions and processes studied. Error bars are removed for ease of reading graph.

The electrical conductivity indicates a thermally activated energy, but the Seebeck coefficient indicates a lack of thermally activated energy due to carrier concentration decreasing with increasing temperature. In an attempt to understand the mobility the following analysis was completed from 600°C to 1000°C, using Equation 27 to calculate the activation energy for mobility, and resulting in Table IV.

$$e^{\frac{-E_\sigma}{k_B T}} = e^{\frac{-E_\alpha}{k_B T}} + e^{\frac{-E_\mu}{k_B T}} \tag{27}$$

E_σ is the activation energy from conductivity, and E_μ is the activation energy for mobility of the carriers. The numbers calculated for E_α are not necessarily activation energy, but can be due to the filling of oxygen vacancies. It can be observed that the mobility is slightly activated with an average of 0.061eV ± 0.017. The magnitudes of the mobility activation energies are reasonable, because the magnitude of both electrical conductivity and Seebeck coefficient do not dramatically decrease or increase.

Table IV. Activation Energy of GITO Samples from 600°C-1000°C

Composition/Process	E_σ (eV)	E_α (eV)	E_μ (eV)
x=0.6 CS	0.015	-0.055	0.07
x=1.0 CS	0.033	-0.073	0.11
x=1.6 CS	0.095	-0.065	0.066
x=0.6 SPS	0.062	-0.029	0.091
x=1.0 SPS	0.013	-0.063	0.076
x=1.6 SPS	0.029	-0.035	0.064

From electrical conductivity and Seebeck coefficient, power factor (PF) can be calculated using Equation 6 mentioned earlier ($PF=\alpha^2\sigma$), and is shown in Figure 20. Error in the power factor calculation is noted to be less than 10%. For comparing the two processes and the mechanisms affected, Figure 21 has power factor normalized by density as a function of increasing temperature. For all samples, power factor increases as

temperature increases. Due to the decrease in absolute thermopower for SPS x=0.6 and x=1.6 consolidated samples, these samples are only slight increase in power factor as compared to their solid state synthesized counterparts. For the SPS x=1.0 sample, the dramatic increase in absolute thermopower, along with the increase in electrical conductivity, allows it to have the highest power factor. There is a slight increase in power factor of the solid state synthesized compositions due to increase in density when comparing the density normalized power factors. This increase is due to an increase in electrical conductivity while not sacrificing thermopower. While the increase in electrical conductivity does increase power factor, it does not account for the reducing quality that condensing with SPS allows.

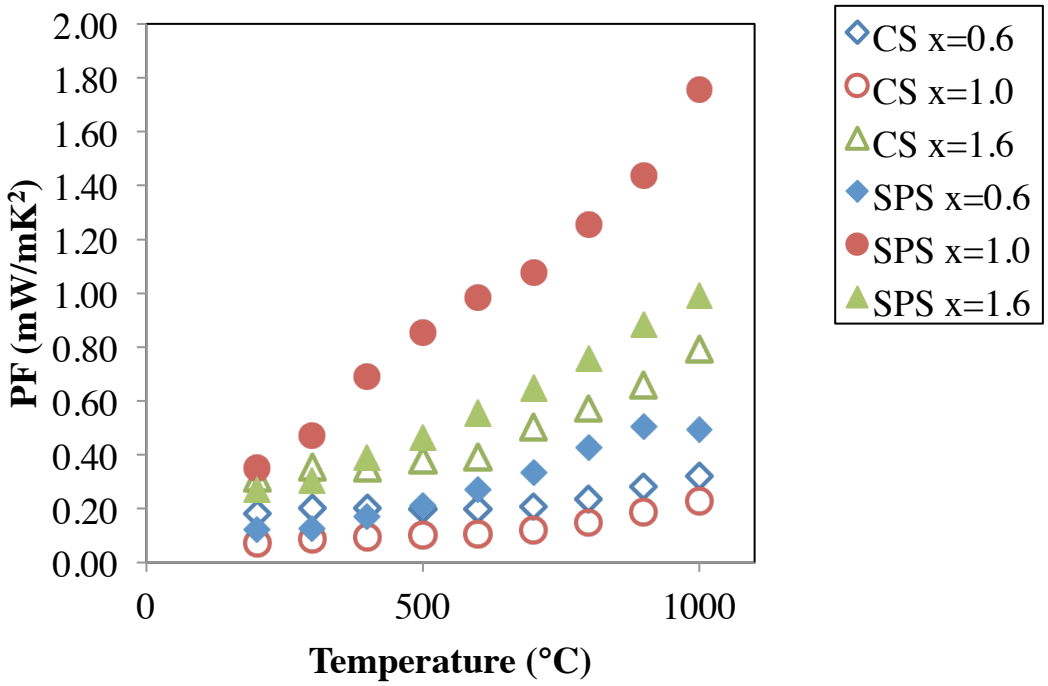

Figure 20. Power factor as a function of temperature.

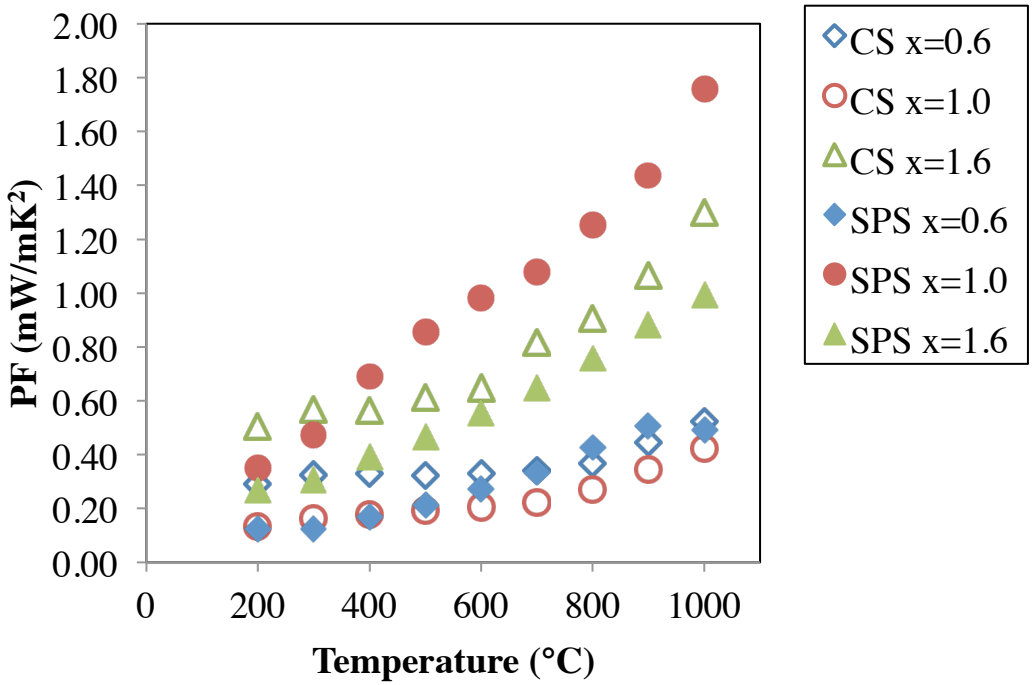

Figure 21. Power factor of pressureless sintered samples normalized and compared to the SPS counter parts as a function of temperature Error bars are removed for ease of reading graph.

5. Thermal Conductivity

Thermal conductivity of the samples were calculated by Equation 19 and shown in Figure 22. Thermal diffusivity and specific heat measurements were given a 2nd order polynomial trendline and recalculated in order to reduce scatter. In general, thermal conductivity for all samples increased with increasing temperature. The increase in thermal conductivity as a function of temperature is attributed to the increase in electrical thermal conductivity (κ_E) via the increase of electrical conductivity. The CS x=1.0 and SPS x=0.6 have the lowest and highest thermal conductivity values at 1000°C, respectively. The SPS consolidated samples have higher thermal conductivity values than the solid state synthesized counterparts. This may be due to both the increase in density of the samples and increase in electrical conductivity when sintered via SPS. Overall, there seems to be no trend in thermal conductivity as a function of composition, but for all samples there seems to be a change in rate of increasing thermal conductivity at 600°C. Figure 23 shows thermal conductivity of the samples when normalized in relation to percent theoretical density. The thermal conductivity values for the x=1 composition

are similar when normalized, but the other compositions do not show that similarity. In general, the pressureless sintered compositions have the thermal conductivity values needed for a good thermoelectric, $\kappa<2W/m*K$.

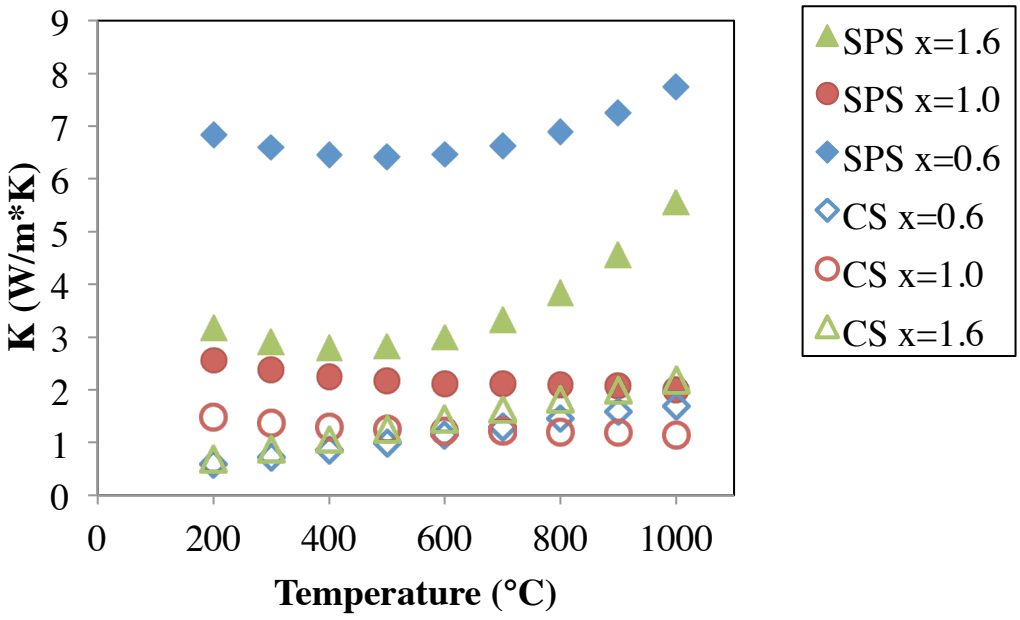

Figure 22. Thermal conductivity as a function of temperature.

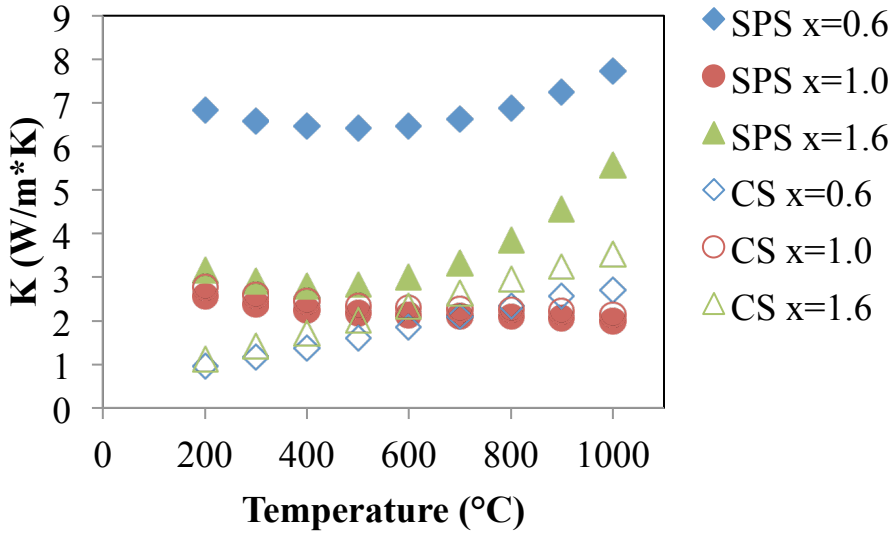

Figure 23. Thermal conductivity normalized to percent theoretical density of SPS compositions as a function of temperature.

6. Figure of Merit, ZT

Using electrical conductivity, Seebeck coefficient, and thermal conductivity the figure of merit value, ZT, can be calculated using Equation 11 noted earlier, and the results are seen in Figure 24. Error in ZT calculation is noted to be less than 5%. For all compositions ZT increases with increasing temperature. For pressureless sintered samples, ZT also increases as function of composition at 1000°C, but the SPS consolidated samples do not have a trend as a function of composition. The highest ZT value calculated was the SPS x=1.0 composition with ZT=1.12 at 1000°C, and the lowest ZT value calculated was the SPS x=0.6 composition with ZT=0.08 at 1000°C. The main components of the dramatic change in ZT are the change in thermopower and thermal conductivity as a function of temperature.

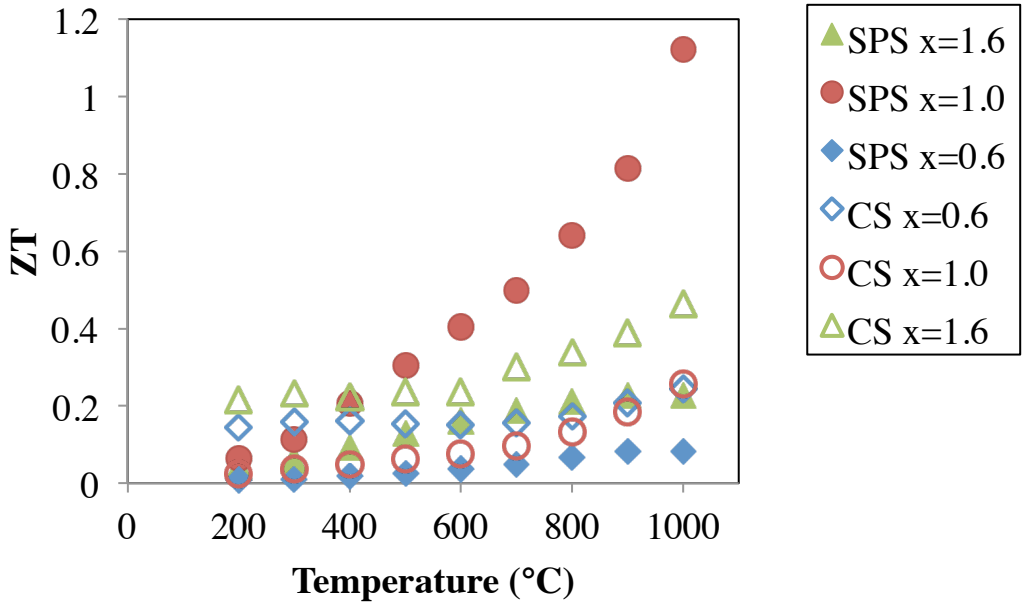

Figure 24. Figure of merit, ZT, as a function of temperature.

Overall GITO is a viable thermoelectric, since it able to have σ>1000S/cm and κ<5W/m*K. While the thermopower is not at the S>150μV/K ideal, the low κ values measured make up for that fault.

P-TYPE THERMOELECTRIC $CA_3CO_4O_9$

A. Background

Due to the fruitful investigation of single crystal $Na_2Co_2O_4$ as a thermoelectric in 1997, cobalt-based oxides became a large topic of interest for thermoelectric usage. Research performed on this family of materials showed many promising thermoelectrics such as Bi-M-Co-O (M=Ca, Sr, Ba). In order to investigate higher performing and more stable thermoelectric cobalt-based oxides, $Ca_3Co_4O_9$ became a material of interest in 2000. $Ca_3Co_4O_{9+\delta}$ was synthesized in 1968, and single crystals of $Ca_3Co_4O_9$ were developed in 1970, but structural analysis and thermoelectric property measurements were not completed until 2001.[36]

$Ca_3Co_4O_9$ has monoclinic symmetry with an incommensurate misfit-structure due to having multiple layers of sub-structures with different compositions, as seen in Figure 25. There are two layers in the structure: a single conductive CdI_2-type hexagonal CoO_2 layer, and a triple insulating rocksalt-type block layer of CoO and CaO compositions. These two layers have common a- and c-axis lattice parameters and β angles, but the b-axis length is different, thus causing the misfit in the structure. The two different b-axis lengths are due to the difference in b-axes of the two layers in the structure, where the rocksalt-type layer has b_1=4.5615Å, and the CdI_2-type layer has b_2=2.8173Å. Due to the layered structure, $Ca_3Co_4O_9$ can also be written as $[Ca_2CoO_3][CoO_2]_{1.62}$.[37]

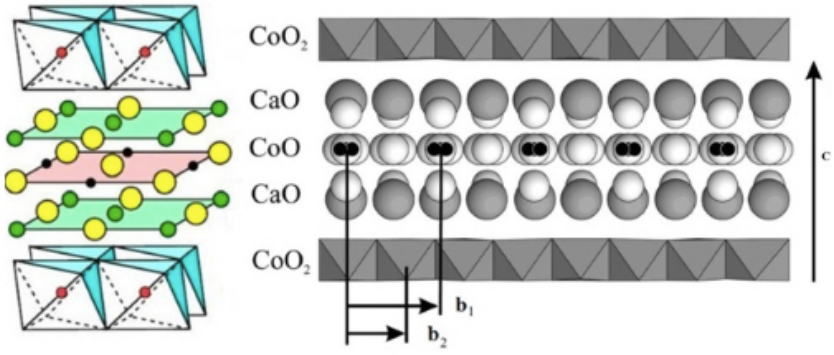

Figure 25. Schematic of the $Ca_3Co_4O_9$ crystal structure.[36]

$Ca_3Co_4O_9$ is not often used in applications with functioning temperatures above 900°C. Figure 26 shows that the $Ca_3Co_4O_9$ is stable in air under 926°C, then has a decomposition reaction of trivalent cobalt oxide (Co_2O_3) into divalent cobalt oxide (CoO) overall creating $Ca_3Co_2O_6$ and CoO. There is another decomposition of $Ca_3Co_4O_9$ at 1026°C, in which the materials decompose to CaO and CoO phases.[38] These decomposition reactions limits sintering temperature and application temperatures. The decomposition of these phases causes a multiple phase material, and diminishes the thermoelectric capabilities of the material.

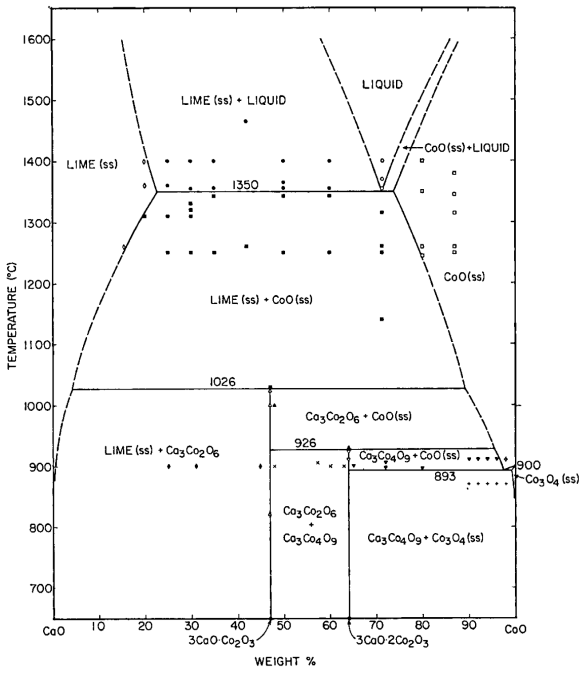

Figure 26. Phase diagram for CoO-cobalt system in air.[37]

The crystallographic anisotropy of the $Ca_3Co_4O_9$ plays a role in its electrical properties. The anisotropy causes the formation of randomly oriented plate-like grains during sintering. By taking advantage of this formation, it is possible to preferentially align the grains using different processes such as spark plasma sintering, microwave texturing, and templated grain growth. Aligning the grains also aligns the conduction planes, which orients the charge flow direction and thus increases electrical conductivity.[39]

Different methods have been used to tailor the thermoelectric properties of $Ca_3Co_4O_9$. Metallic oxide doping and using different synthesis processes are currently the most common routes of research. Commonly cations used for this type of doping are bismuth, strontium, and silver. Bismuth has been shown to decrease thermal conductivity, and increase both thermopower and electrical conductivity. This is due to the increase in ion size from calcium to bismuth, and an increase in carrier mobility.[40] Small amounts of strontium ($x>0.10$) have been seen to decrease thermal conductivity with little change in electrical conductivity and thermopower. These effects are once again due to the increase in phonon scattering by increasing the ionic size of the cation.[41,42] The most favorable ZT results seem to be from silver doping; reaching to ~0.5 at 1000K. Electrical conductivity increases from silver doping due to both increase in carrier concentration and mobility, but thermopower has been shown to either increase or decrease. Thermal conductivity also decreases with silver doping due to the increase in mass from calcium to silver. Silver has also been investigated as a secondary metallic phase along with silver doping with allows for both increases in electrical conductivity and thermopower instead of the usual increase in electrical conductivity and decrease in thermopower from adding secondary metallic phases.[43]

Due to the anisotropic nature of $Ca_3Co_4O_9$ processing conditions are able to have a large impact on thermoelectric properties. Solid state synthesis causes large processing times at high temperatures, which usually yields highly porous samples with non-stoichiometric phases, and less homogeneity as compared to other processing methods, but is usually used as the benchmark to compare any changes in thermoelectric properties. Spark plasma sintering is a commonly used processing method in research due to rapid synthesizing or sintering rates, and usually causes an increase in ZT values due to the increase in electrical conductivity.[44] Soft chemical processes such as sol-gel and polymer solution synthesis have been shown to increase ZT values by decreasing secondary phases that can occur in solid state synthesis.[45] The Pechini method has also been investigated to achieve pure $Ca_3Co_4O_9$ materials, but no testing has confirmed that only using this method does increase ZT values.[46] The Pechini method and SPS have been combined to reach ZT values of ~0.25 at 1073K for undoped $Ca_3Co_4O_9$.[47]

The goal of this research is to see the effects on $Ca_3Co_4O_9$ thermoelectric properties by doping with metallic oxides, and changing density via sintering conditions.

B. **Synthesis**

Samples of $Ca_{3-x}Sr_xCo_4O_9$ (x=0.035, 0.053, 0.070) and $Ca_{3-y}Ag_yCo_4O_9$ (y=0.05, 0.10, 0.15, 0.25, 0.30) were prepared using solid state synthesis techniques. Powders were synthesized and calcined at TAM Ceramics (Niagara Falls, NY). Pellets were pressed together with 5% PVA binder solution, and heated in high-density alumina crucibles at 900°C for 20hrs and quenched in air. The pellets were placed on a powder bed of the same composition during firing in order to prevent contamination from the alumina crucibles. Samples of the same composition were made at TAM Ceramics and fired at 1100°C for 4hrs in air. Table V and Table VI summarize the doping and processing schemes for Ca-Co-based materials studied.

Table V. Doping and Processing Scheme of $Ca_3Co_4O_9$ samples sintered at 900°C.

Sample Label	Composition	Calcine Temperature (°C)	Calcine time (hr)	Sintering Temperature (°C)	Sintering time (hr)
x=0.0	$Ca_3Co_4O_9$	950	4	900	20
x=0.018	$Ca_{2.972}Sr_{0.018}Co_4O_9$	950	4	900	20
x=0.053	$Ca_{2.947}Sr_{0.053}Co_4O_9$	950	4	900	20
x=0.070	$Ca_{2.93}Sr_{0.07}Co_4O_9$	950	4	900	20
y=0.05	$Ca_{2.95}Ag_{0.05}Co_4O_9$	900	4	900	20
y=0.1	$Ca_{2.9}Ag_{0.1}Co_4O_9$	900	4	900	20
y=0.15	$Ca_{2.85}Ag_{0.15}Co_4O_9$	900	4	900	20
y=0.25	$Ca_{2.75}Ag_{0.25}Co_4O_9$	900	4	900	20
y=0.30	$Ca_{2.7}Ag_{0.3}Co_4O_9$	900	4	900	20

Table VI. Doping and Processing Scheme of $Ca_3Co_4O_9$ Samples Sintered at 1100°C

Sample Label	Composition	Calcine Temperature (°C)	Calcine time (hr)	Sintering Temperature (°C)	Sintering time (hr)
x=0.0	$Ca_3Co_4O_9$	900	4	1100	4
x=0.018	$Ca_{2.972}Sr_{0.018}Co_4O_9$	900	4	1100	4
x=0.053	$Ca_{2.947}Sr_{0.053}Co_4O_9$	900	4	1100	4
x=0.070	$Ca_{2.93}Sr_{0.07}Co_4O_9$	900	4	1100	4
y=0.05	$Ca_{2.95}Ag_{0.05}Co_4O_9$	900	4	1100	4
y=0.1	$Ca_{2.9}Ag_{0.1}Co_4O_9$	900	4	1100	4
y=0.15	$Ca_{2.85}Ag_{0.15}Co_4O_9$	900	4	1100	4
y=0.25	$Ca_{2.75}Ag_{0.25}Co_4O_9$	900	4	1100	4
y=0.30	$Ca_{2.7}Ag_{0.3}Co_4O_9$	900	4	1100	4

C. Results and Discussion

1. XRD

X-ray diffraction patterns are compiled: Sr doped and sintered at 900°C is Figure 27, Sr doped and sintered at 1100°C is seen in Figure 28, Ag doped and sintered at 900°C is seen in Figure 29, and Ag doped and sintered at 1100°C is seen in Figure 30. Diffraction patterns used are 00-062-0692, 04-001-2617, 01-078-5623, 04-010-0812, and 04-015-6966. All undoped samples have a small phase formation of another Ca-Co-O phase: $Ca_3Co_2O_6$. For the strontium doped compositions, the samples are majority single phase, with very little secondary $Ca_3Co_2O_6$ and $SrCo_{12}O_{19}$ peaks at 900°C and much more pronounced secondary peaks at 1100°C. This indicates that the majority of the Sr has been incorporated into the structure. For silver doped samples, metallic silver was observed as a secondary phase for all samples. Also for the samples at 1100°C, the silver doped samples may have made more of a composite-type structure due to silver melting above 950°C. Samples that were sintered at 1100°C should have more pronounced secondary phases, since there are two decomposition reactions for $Ca_3Co_4O_9$ that occur at 926°C and 1026°C. More peaks did develop in the patterns, though it is difficult to distinguish the decomposition peaks from the primary $Ca_3Co_4O_9$ peaks.

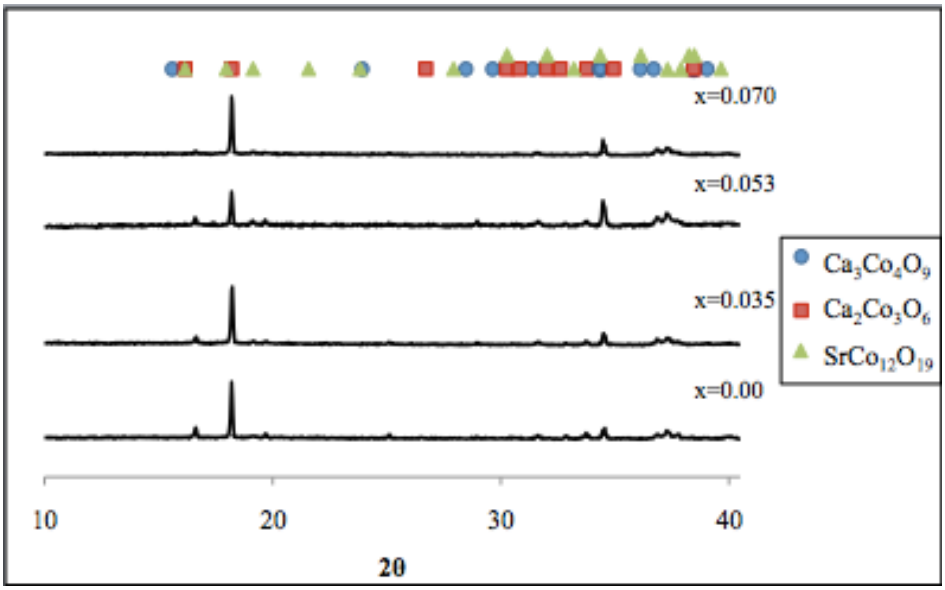

Figure 27. X-ray diffraction patterns of $Ca_{3-x}Sr_xCo_4O_9$ compositions sintered at 900°C. Peaks marked (o) are $Ca_3Co_4O_9$, (□) peaks are $Ca_3Co_2O_6$, and (Δ) are $SrCo_{12}O_{19}$.

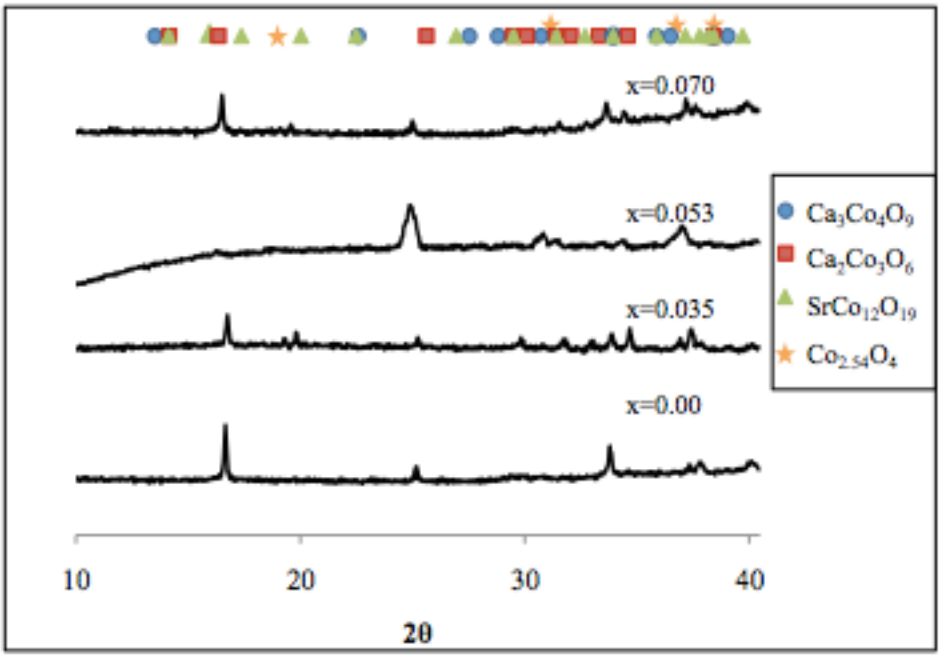

Figure 28. X-ray diffraction patterns of $Ca_{3-x}Sr_xCo_4O_9$ compositions sintered at 1100°C. Peaks marked (o) are $Ca_3Co_4O_9$, (□) peaks are $Ca_3Co_2O_6$, (Δ) are $SrCo_{12}O_{19}$, and are (★) are $Co_{2.54}O_4$.

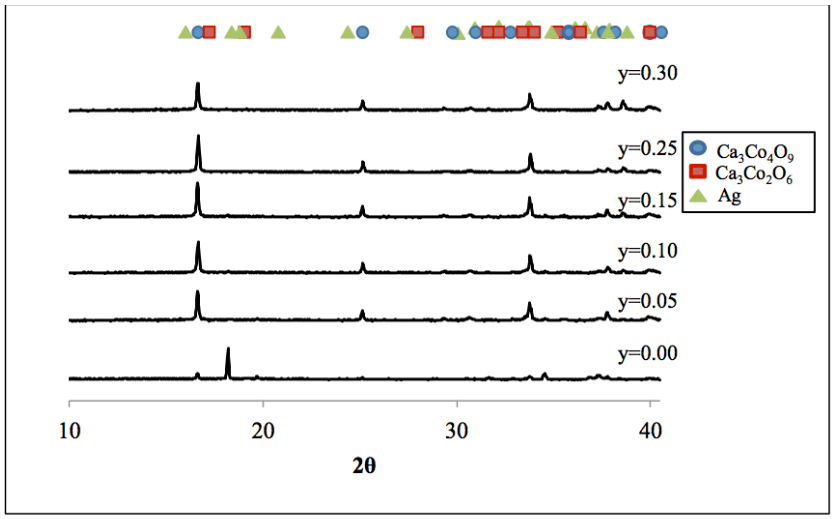

Figure 29. X-ray diffraction patterns of $Ca_{3-y}Ag_yCo_4O_9$ compositions sintered at 900°C. Peaks marked (o) are $Ca_3Co_4O_9$, (□) peaks are $Ca_3Co_2O_6$, and (Δ) are Ag.

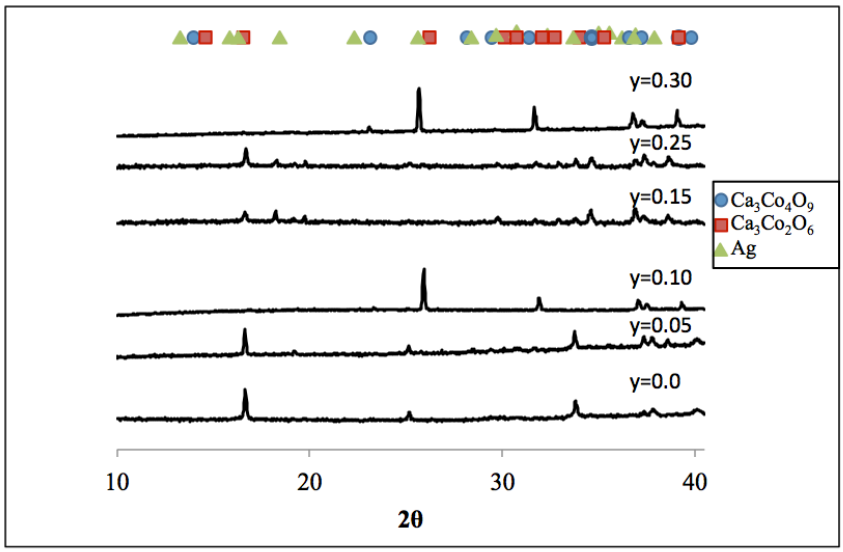

Figure 30. X-ray diffraction patterns of $Ca_{3-y}Ag_yCo_4O_9$ compositions sintered at 1100°C. Peaks marked (o) are $Ca_3Co_4O_9$, (□) peaks are $Ca_3Co_2O_6$, and (Δ) are Ag.

2. Density

Processing parameters, compact density results, and specific surface area (SSA) of the calcined powders are compiled in Table VII. Densities of sintered compacts were determined using the Archimedes method, and SSA was determined using BET. Density generally increased with doping and increased sintering temperature. The percent of

theoretical density (ρ_{Th}) cannot be determined for the samples sintered at 1100°C due to the multiphase composition of the samples. SSA of calcined powders increased for Sr doping and decreased for Ag doping. The densities of the samples sintered at 900°C are lower than expected, Constantinescu *et al*. observed theoretical densities ranging from 75% to 79%.[48] The lower densities may be due to low pressing pressures to form the compacts before sintering.

Table VII. Density and BET Measurements of Ca-Co-O-based Materials Studied

Composition	Temperature Sintered (°C)	Density (g/cm^3)	% Open Porosity	ρ_{Th} (%)	SSA (m^2/g)
$Ca_3Co_4O_9$	900	1.97	55.84	46.7	13.4446
$Ca_{2.972}Sr_{0.035}Co_4O_9$	900	2.09	52.83	44.73	30.1761
$Ca_{2.947}Sr_{0.053}Co_4O_9$	900	2.07	53.83	44.39	29.7987
$Ca_{2.93}Sr_{0.07}Co_4O_9$	900	2.11	52.52	45.00	34.5394
$Ca_{2.95}Ag_{0.05}Co_4O_9$	900	2.16	52.25	46.25	2.8874
$Ca_{2.9}Ag_{0.1}Co_4O_9$	900	2.11	53.65	45.05	2.9489
$Ca_{2.85}Ag_{0.15}Co_4O_9$	900	2.20	52.12	47.00	2.9487
$Ca_{2.75}Ag_{0.25}Co_4O_9$	900	2.32	50.25	49.61	2.6086
$Ca_{2.7}Ag_{0.3}Co_4O_9$	900	2.18	53.68	46.65	2.6372
$Ca_3Co_4O_9$	1100	3.29	29.09	N/A	16.26
$Ca_{2.972}Sr_{0.035}Co_4O_9$	1100	3.29	22.73	N/A	28.87
$Ca_{2.947}Sr_{0.053}Co_4O_9$	1100	3.67	16.08	N/A	36.48
$Ca_{2.93}Sr_{0.07}Co_4O_9$	1100	3.76	14.79	N/A	47.06
$Ca_{2.95}Ag_{0.05}Co_4O_9$	1100	3.34	19.04	N/A	3.17
$Ca_{2.9}Ag_{0.1}Co_4O_9$	1100	3.07	29.53	N/A	3.36
$Ca_{2.85}Ag_{0.15}Co_4O_9$	1100	3.33	18.71	N/A	3.36
$Ca_{2.75}Ag_{0.25}Co_4O_9$	1100	3.22	28.49	N/A	3.62
$Ca_{2.7}Ag_{0.3}Co_4O_9$	1100	3.36	29.41	N/A	3.43

3. SEM

Microstructural images of fractured surfaces of all sintered samples were taken with a scanning electron microscope. Images of each composition were taken of all compositions and sintering temperatures, and can be seen in Figure 31 and Figure 32. Within each sintering temperature there is little grain structure change as a function of doping level, but 900°C sintered samples have more defined grains as compared to the 1100°C samples. Grains are platelet shaped and randomly oriented when sintered at 900°C, with many open areas between grains. At 1100°C, grains are thinner platelets, and have become more interconnected with a higher degree of orientation. This microstructure contains many interconnected grains, but small open sections with an overall higher degree of densification. These SEM images generally confirm the density changes noted previously. The lack of interconnected grain boundaries in the samples indicates vapor transport as the sintering mechanism. This sintering mechanism allows neck growth of grain boundaries but does not cause densification, which correlates to the low theoretical densities observed in the samples.

(a) 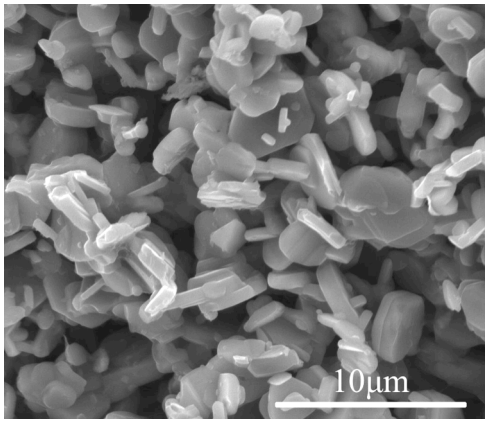

(b) 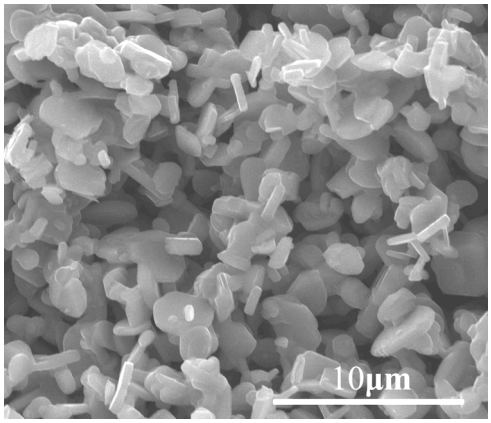

(c) 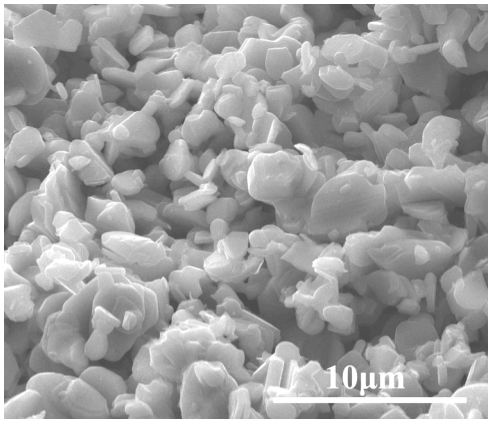

(d) 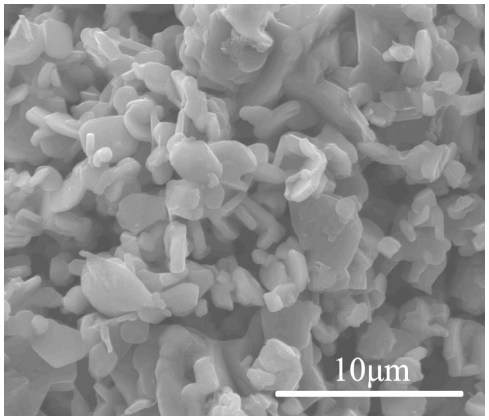

(e) 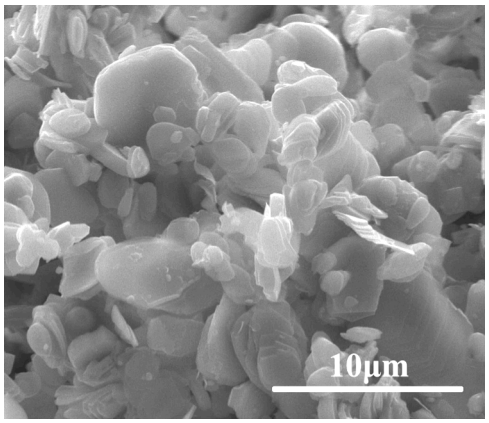

(f) 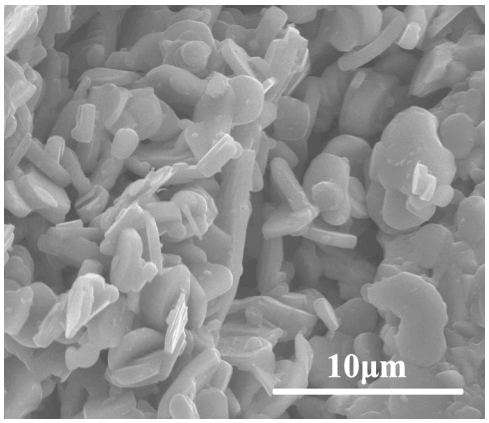

(g) 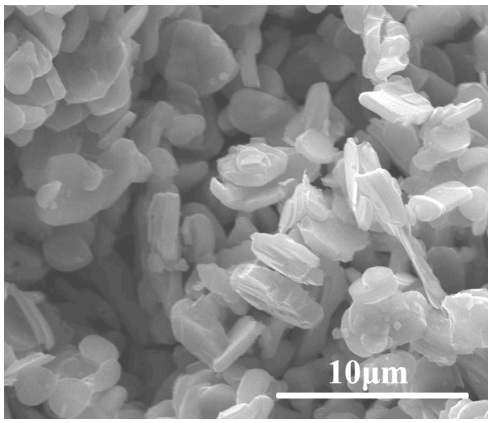

(h) 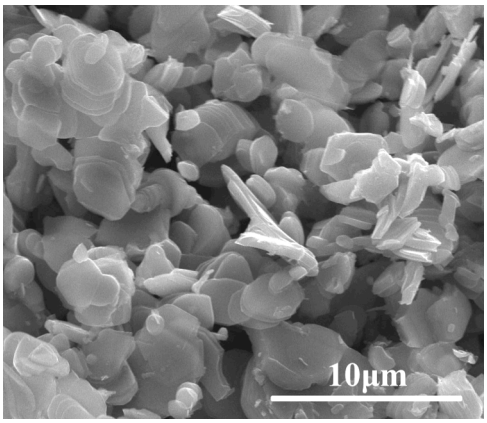

(i) 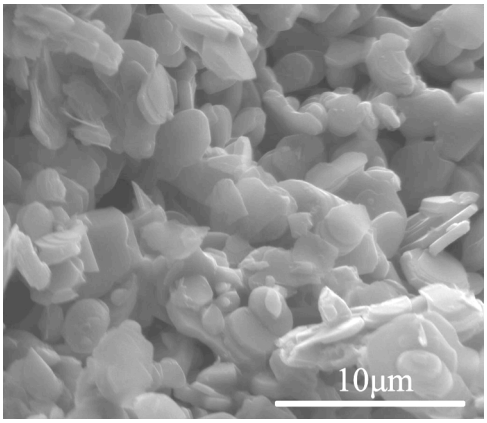

Figure 31. SEM images of $Ca_3Co_4O_9$ compositions sintered at 900°C: a) $Ca_3Co_4O_9$, b) $Ca_{2.972}Sr_{0.035}Co_4O_9$, c) $Ca_{2.947}Sr_{0.053}Co_4O_9$, d) $Ca_{2.93}Sr_{0.070}Co_4O_9$, e) $Ca_{2.95}Ag_{0.05}Co_4O_9$, f) $Ca_{2.90}Ag_{0.10}Co_4O_9$, g) $Ca_{2.85}Ag_{0.15}Co_4O_9$, h) $Ca_{2.75}Ag_{0.25}Co_4O_9$, i) $Ca_{2.70}Ag_{0.30}Co_4O_9$.

(a) 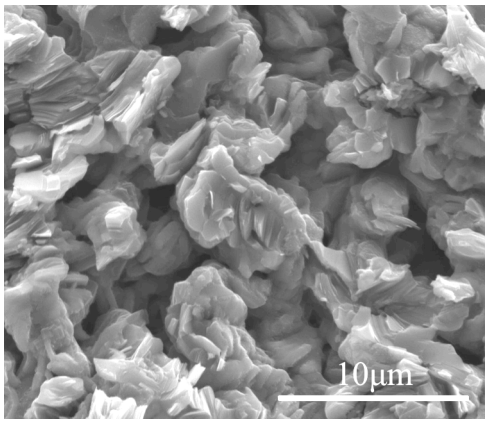

(b) 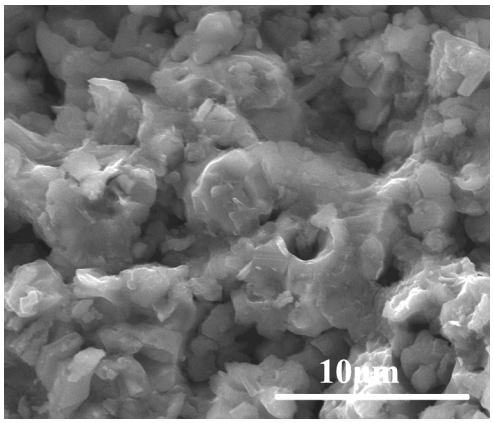

(c) 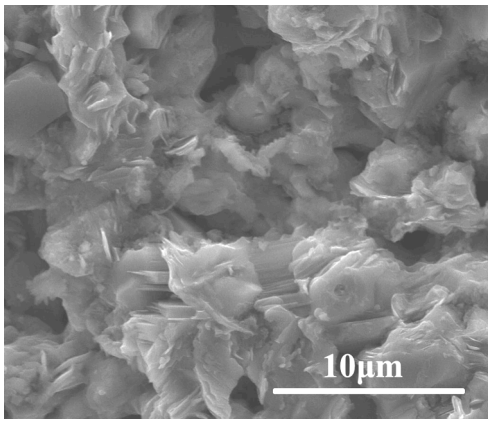

(d) 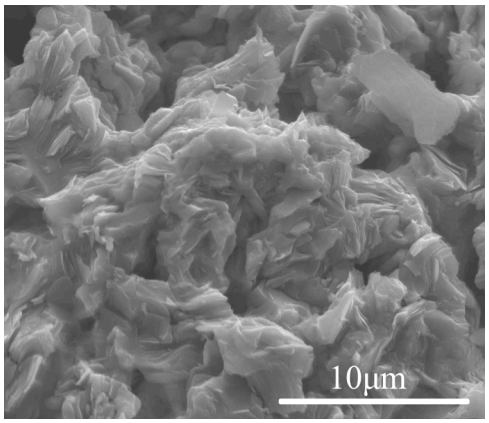

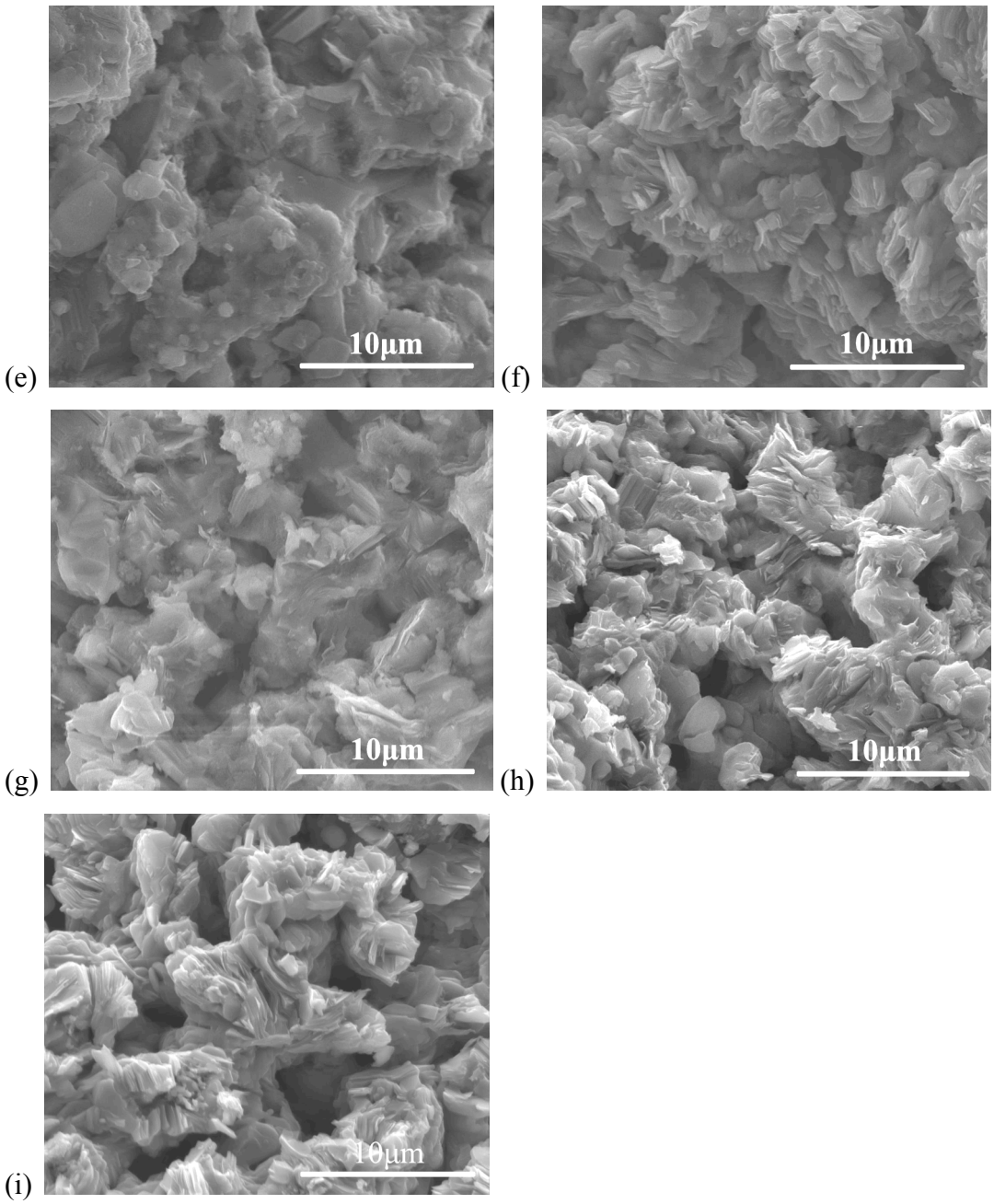

Figure 32. SEM images of $Ca_3Co_4O_9$ compositions sintered at 1100°C: a) $Ca_3Co_4O_9$, b) $Ca_{2.972}Sr_{0.035}Co_4O_9$, c) $Ca_{2.947}Sr_{0.053}Co_4O_9$, d) $Ca_{2.93}Sr_{0.070}Co_4O_9$, e) $Ca_{2.95}Ag_{0.05}Co_4O_9$, f) $Ca_{2.90}Ag_{0.10}Co_4O_9$, g) $Ca_{2.85}Ag_{0.15}Co_4O_9$, h) $Ca_{2.75}Ag_{0.25}Co_4O_9$, i) $Ca_{2.70}Ag_{0.30}Co_4O_9$.

4. Electrical Conductivity, Seebeck Coefficient, and Power Factor

Direct current electrical conductivity (σ) was measured from 200-800°C for all $Ca_3Co_4O_9$-based samples, and are shown in Figure 33 and Figure 34, respectively. For the Sr-doped samples electrical conductivity is seen to increase as temperature increases,

indicating semimetallic behavior. Samples sintered at 1100°C have higher conductivities than samples sintered at 900°C, except for x=0.035 which has more pronounced secondary phases than the other compositions and thus could have decreased conductivity. The increase in conductivity may be due to the decreases in open porosity, and alignment of grains. In general, conductivity increases with Sr content, and the trends are more pronounced in the samples sintered at 1100C. The increase in conductivity as Sr content increases is due to the increase in dimensions of the rocksalt substructure. Sr^{2+} is a larger ion than Ca^{2+}, which causes the lattice parameters of the substructure to increase.[49] For the Ag-doped samples the electrical conductivity also increases as temperature increases. The samples that were sintered at 1100°C also have greater electrical conductivity values than samples sintered at 900°C, and are possibly caused by the decrease in open porosity and increase in grain orientation. While the 900°C samples have increasing electrical conductivity with increasing Ag concentration, the 1100°C samples have no trend as concentration increases. The increasing conductivity may be due to more Ag metallic ions being between the grains, thus connecting the cobaltite grains and decreasing grain boundary resistance, and was also observed in work completed by Wang *et al*.[50]

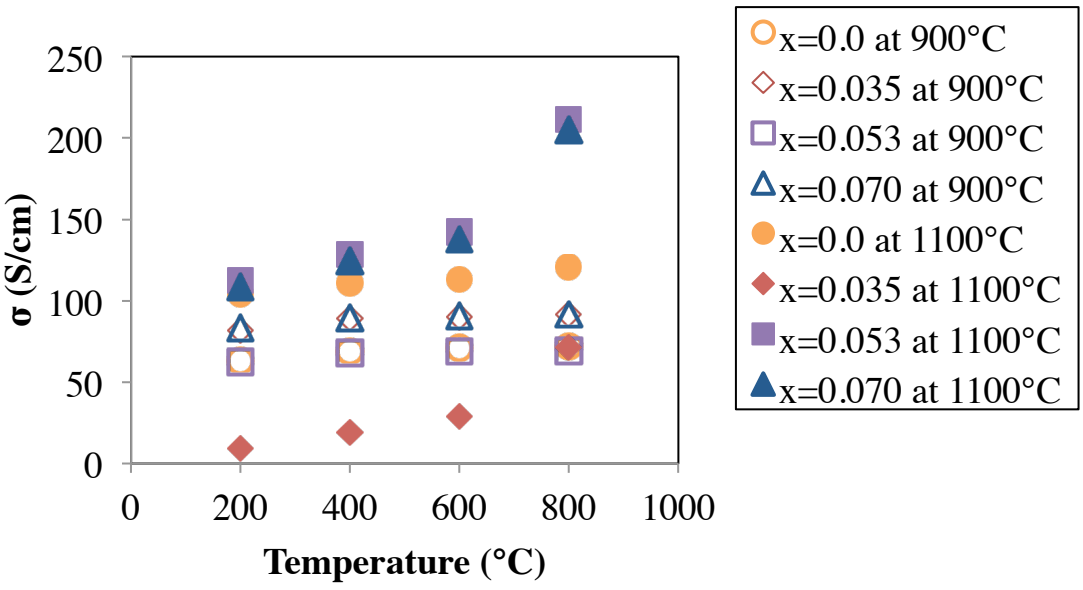

Figure 33. Electrical conductivity results for $Ca_{3-x}Sr_xCo_4O_9$.

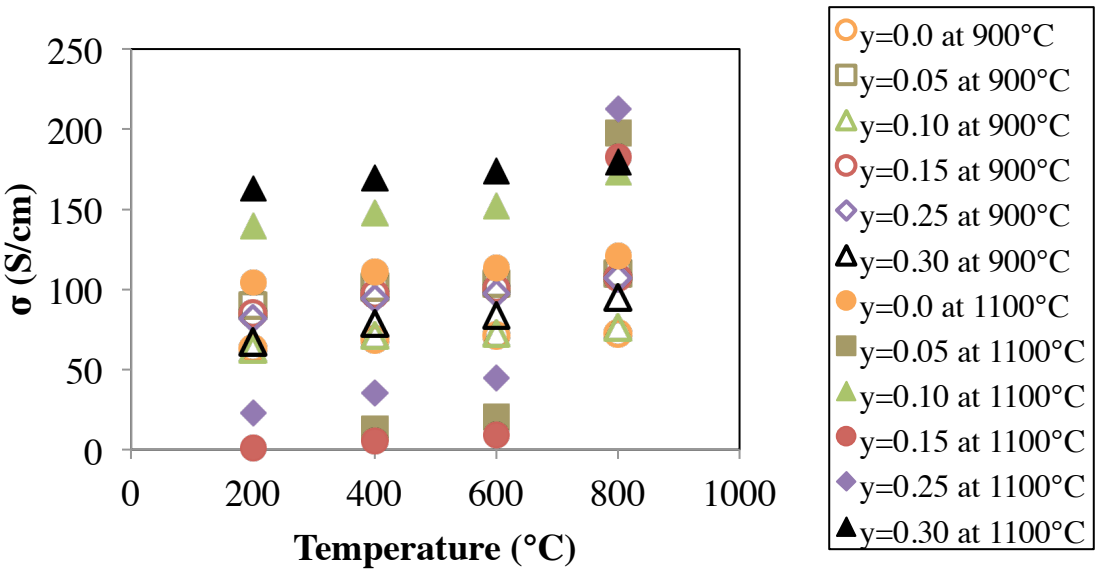

Figure 34. Electrical conductivity results for $Ca_{3-y}Ag_yCo_4O_9$.

Seebeck coefficient (α) was measured simultaneously from 200-800°C for all samples, and shown in Figure 35 and Figure 36, respectively. The Seebeck coefficient is positive, which indicate holes are the majority carriers in the system. The magnitude of the Seebeck coefficient increases with temperature, which indicates either a decrease in carrier concentration, or an increase in mobility of the carriers with increasing temperature. Thermopower does not seem to correlate with Sr content nor sintering temperature. Thermopower increases as Ag content increases up to y=0.15, and then decreases through y=0.30. The initial increase may be due to changing valence states of cobalt.[51] The decrease as Ag is continually increases may be due to either an increase in carrier concentration, or due to the additional thermoelectric voltage from the Ag metal that is present as a secondary phase. The thermopower for Ag is negative, which would overall decrease the thermopower of the samples as Ag content increases. The difference in sintering temperature does not seem to show any trend, but it can be seen that the range of thermopower values is larger for the samples sintered at 1100°C.

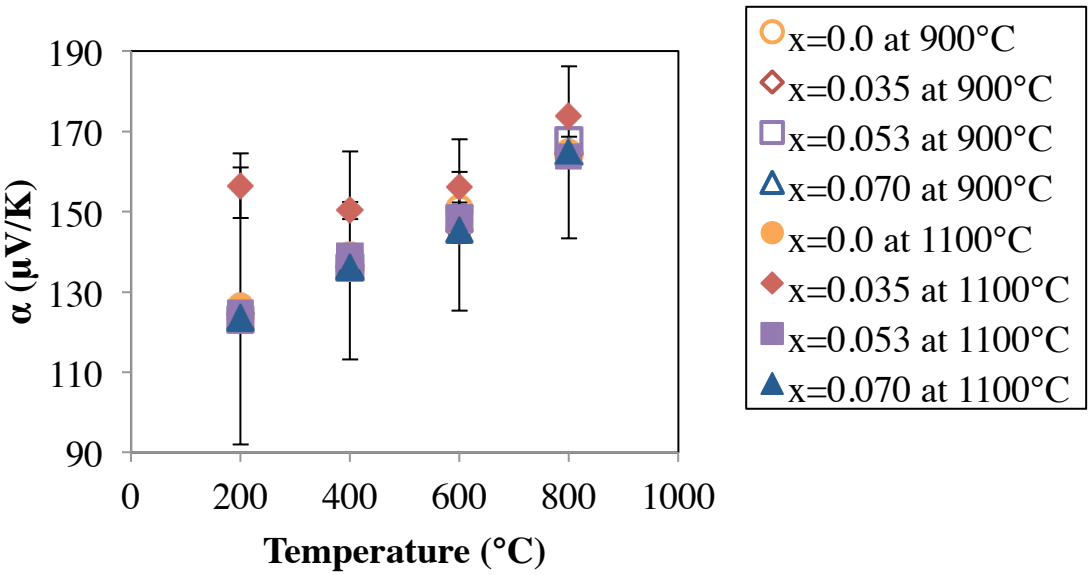

Figure 35. Thermopower results for $Ca_{3-x}Sr_xCo_4O_9$.

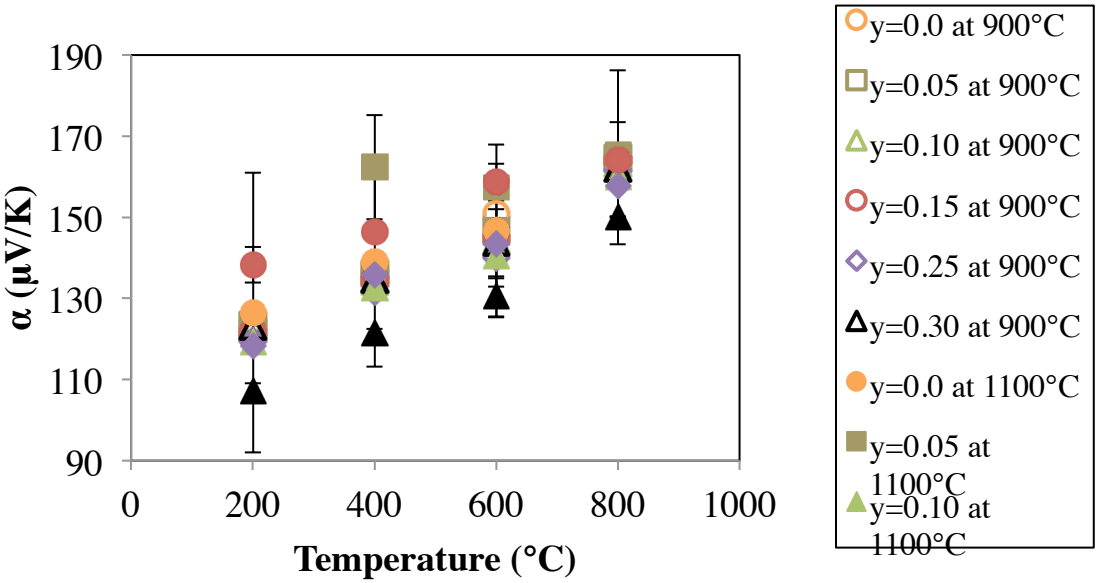

Figure 36. Thermopower results for $Ca_{3-y}Ag_yCo_4O_9$.

The thermopower indicates a possible thermally activated energy for these materials. In an attempt to understand this, the following analysis was completed for the entire temperature range. The compositions sintered at 900°C will be analyzed due to the higher level of phase purity as compared to the compositions sintered at 1100°C. The activation energies can be derived, and are seen in Table VIII and Table IX. It can be

observed that the mobility is activated, and is changing with composition. It can be observed that electrical conductivity is not thermally activated, but there is activation energy stemming from the Seebeck coefficient. The magnitudes of the mobility activation energies are reasonable, because the magnitude of both electrical conductivity and Seebeck coefficient do dramatically increase for Ag doped compositions, the Sr doped compositions have increase less in electrical conductivity, but do increase in thermopower.

Table VIII. Activation Energy of $Ca_{3-x}Sr_xCo_4O_9$ Samples

Composition	E_σ (eV)	E_α (eV)	E_μ (eV)
x=0	0.010	0.033	-0.023
x=0.035	0.001	0.030	-0.029
x=0.053	0.001	0.035	-0.034
x=0.070	0.001	0.032	-0.031

Table IX. Activation Energy of $Ca_{3-y}Ag_yCo_4O_9$ Samples

Composition	E_σ (eV)	E_α (eV)	E_μ (eV)
y=0.05	0.014	0.032	-0.018
y=0.10	0.014	0.031	-0.017
y=0.15	0.016	0.032	-0.016
y=0.25	0.018	0.032	-0.014
y=0.30	0.024	0.030	-0.06

From the electrical conductivity and thermopower, the power factor can be calculated and is seen in Figure 37 and Figure 38. Error in power factor is less than 5%. Power factor ranges from ~0.20-0.60mW/m*K^2 at 800°C. For both doping schemes, the power factor is larger for the samples sintered at 1100°C than samples sintered at 900°C. For all samples, power factor increases as temperature increases. There seems to be no trend of power factor as a function of doping, this is due to the wide range of electrical

conductivity results, which can be due to the changes caused by different secondary phases in the compositions.

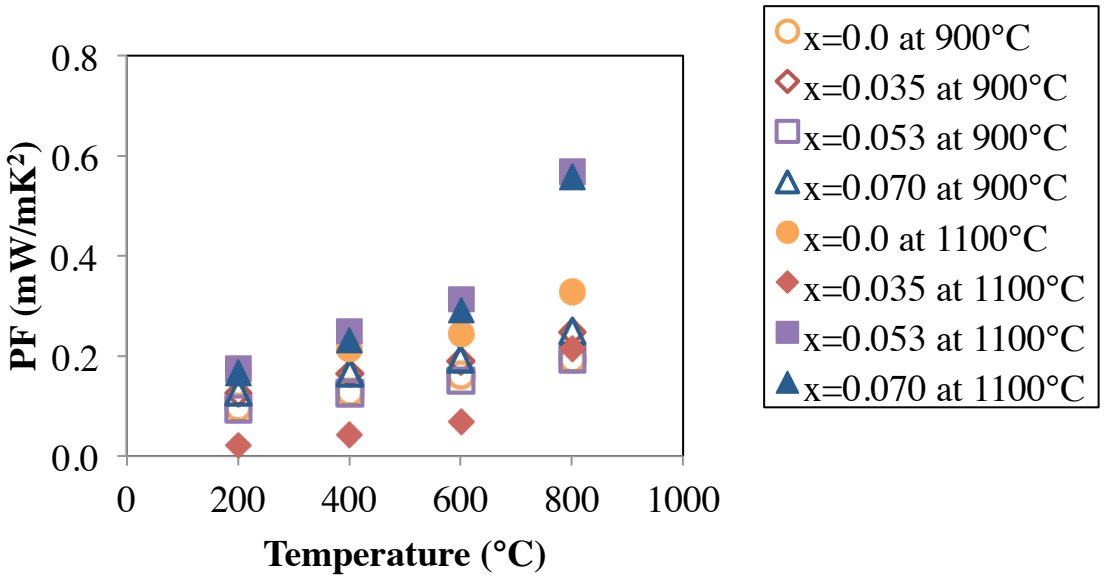

Figure 37. Power factor results for $Ca_{3-x}Sr_xCo_4O_9$.

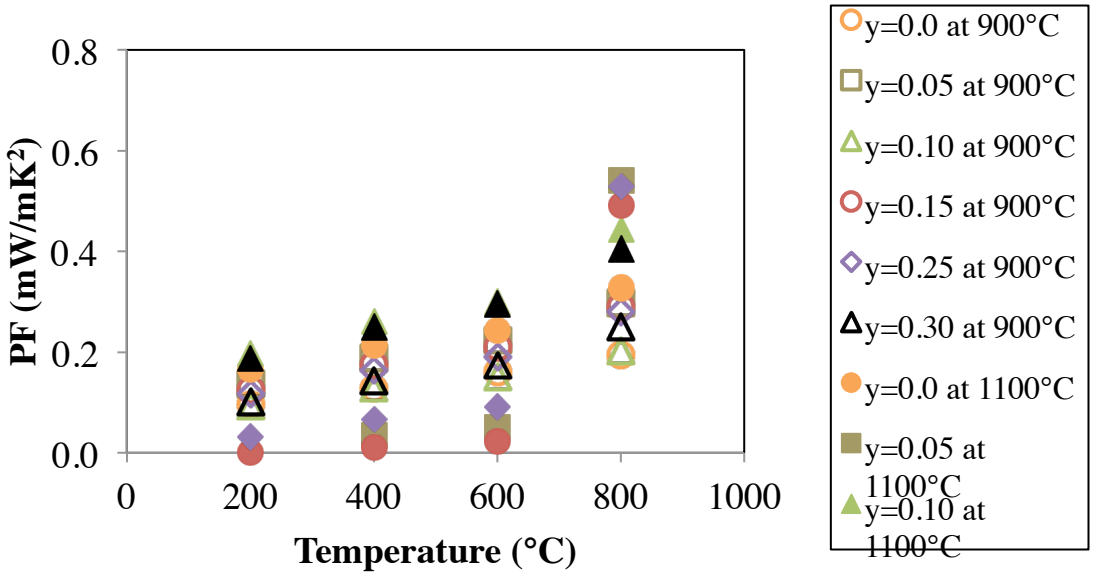

Figure 38. Power factor results for $Ca_{3-y}Ag_yCo_4O_9$.

5. Thermal Conductivity

Thermal conductivity was measured from 200°C-800°C, and can be seen in Figure 39 and Figure 40. Thermal diffusivity and specific heat measurements were given a 2nd order polynomial trendline and recalculated to reduce scatter. For compositions sintered at 900°C, the thermal conductivity overall stayed constant, while the samples sintered at 1100°C decreased with increasing temperature. The trend for the compositions sintered at 900°C is consistent with literature, but it is unknown why the thermal conductivity is decreasing as temperature increases for the compositions sintered at 1100°C, and will need to be further researched.[52] For all compositions, thermal conductivity is larger for samples sintered at 1100°C as compared to 900°C. This increase may be due to the increase in density as a function of sintering temperature, and a possible increase in electrical thermal conductivity (κ_E) due to the increase in electrical conductivity.

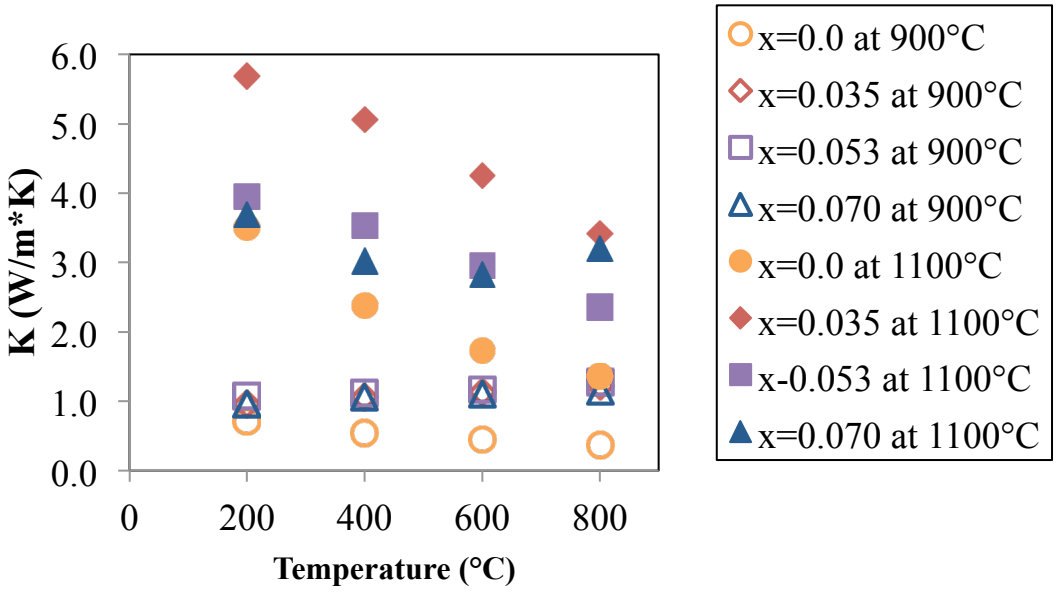

Figure 39. Thermal conductivity results for $Ca_{3-x}Sr_xCo_4O_9$

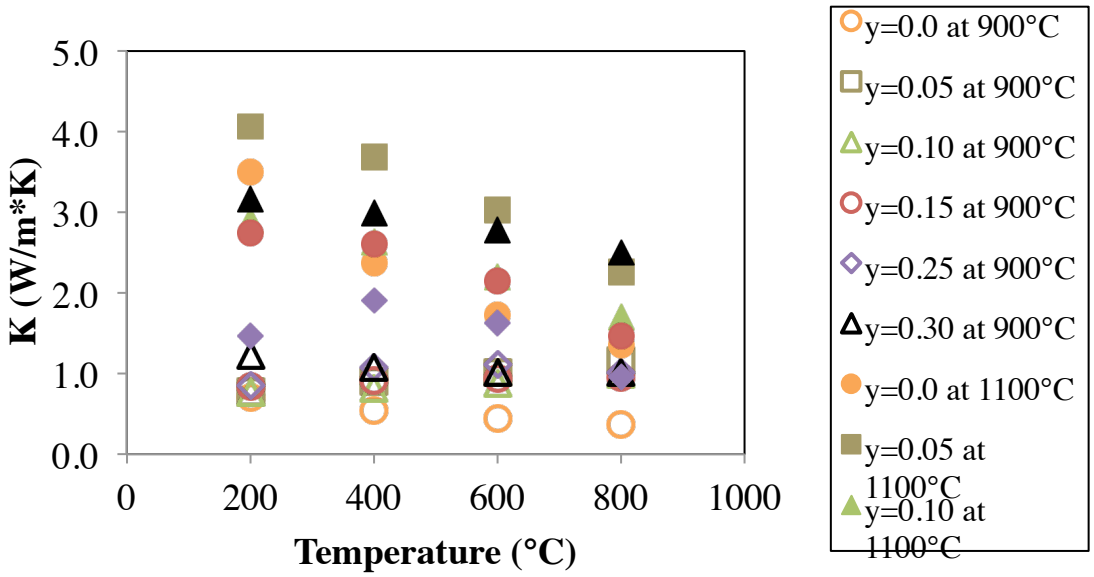

Figure 40. Thermal conductivity results for $Ca_{3-y}Ag_yCo_4O_9$.

6. Figure of Merit, ZT

From thermopower, electrical conductivity, and thermal conductivity the figure of merit value ZT can be calculated, and the results are seen in Figure 41 and Figure 42. Error in ZT is calculated to be less than 5%. For all samples ZT increases with increasing temperature. There is no definitive trend for ZT as a function of sintering temperature. The highest ZT value for compositions sintered at 900°C is the undoped, x=0.0, composition at 0.56. The highest ZT value for compositions sintered at 1100°C is the y=0.25, $Ca_{2.75}Ag_{0.25}Co_4O_9$, composition at 0.59. The main cause for the higher ZT values is due to the lower thermal conductivity values compared to the other compositions. Overall the silver doped compositions have a higher average ZT value as compared to the strontium doped compositions.

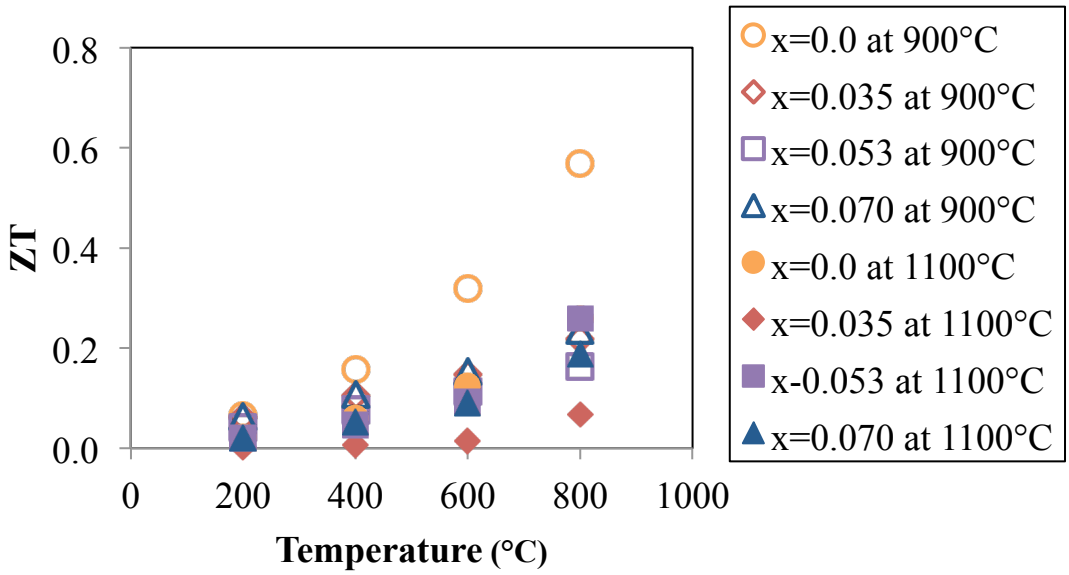

Figure 41. Figure of Merit, ZT, results for $Ca_{3-x}Sr_xCo_4O_9$

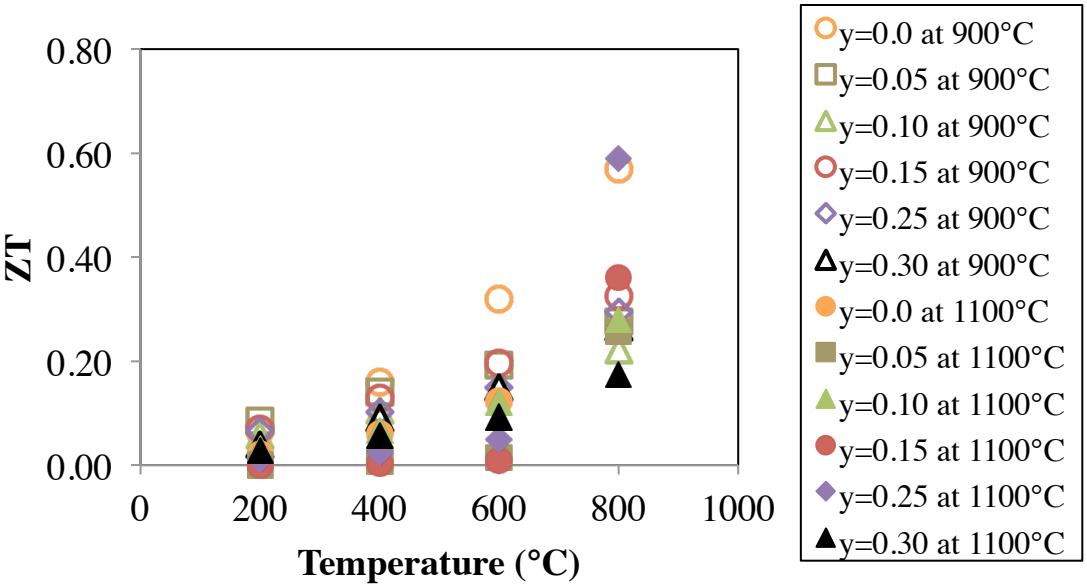

Figure 42. Figure of Merit, ZT, results for $Ca_{3-y}Ag_yCo_4O_9$.

THERMOELECTRIC GENERATOR DESIGN AND ANALYSIS

A. TEG Design

Thermoelectric oxide generators are generally composed in one of two ways: unileg module or π module. Unilegs are composed of one thermoelectric element, either n-type or p-type, whereas π modules have both n-type and p-type thermoelectric elements, see Figure 43. For both styles, the unit has to be electrically in series and thermally in parallel to be most effective. To increase the voltage that is produced, multiple units can be connected in series by a conductive metal, typically silver.[53] Besides the thermoelectric material and the conductive connector, a binder and substrate are needed. The binding material is used to bind the thermoelectric leg and connector and possible wire hookups for testing purposes; silver paste is usually used since it has the same electrical properties as the commonly used silver foil. For substrates a ceramic is usually used to give stability to the thermoelectric legs and withstand higher temperatures that oxide TEGs can attain without loosing mechanical integrity.[54, 55, 56]

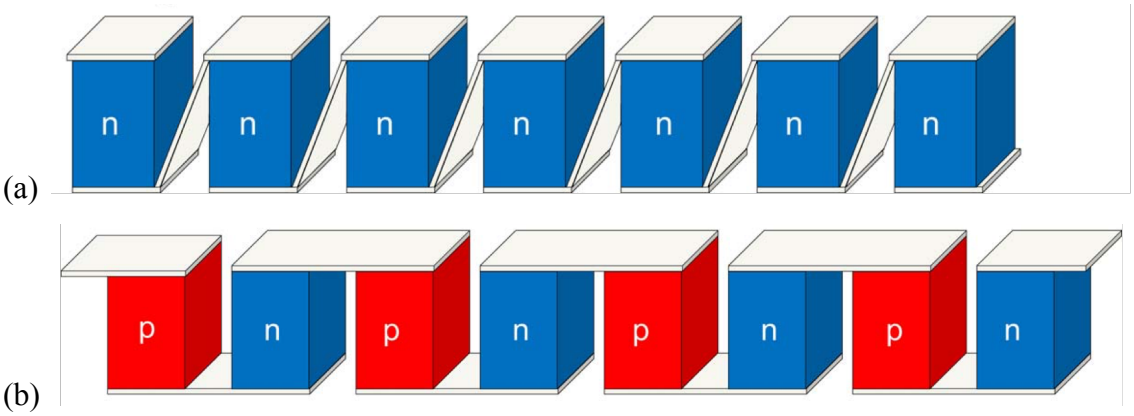

Figure 43. Schematics of (a) unileg and (b) π-shaped thermoelectric modules.

The π module design was chosen in order to determine how well the n-type and p-type materials researched would function in a thermoelectric generator. To be consistent with literature, silver paste, silver foil, and alumina were chosen for the metallic bond, metal connection, and substrate, respectively. The n-type composition chosen was the

SPS consolidated $Ga_2In_6Sn_2O_{16}$, and the p-type composition chosen was the $Ca_{2.93}Sr_{0.070}Co_4O_9$ sintered at 1100°C. These compositions were chosen for their favorable electrical properties.

B. **Determining the Effectiveness of a Thermoelectric Generator**

In order to determine how well the TEG performs, calculations need to be made. Equations 28-36 were used to determine thermoelectric properties, power, and efficiency results of the TEG fabricated. Variables include open circuit voltage (V_O), Short circuit voltage (V_S), open circuit current (I_O), short circuit current (I_S), cold side temperature (T_C), hot side temperature (T_H), temperature difference (ΔT), hot side heat flow (q_H), cold side heat flow (q_C), distance between contacts (l), cross sectional area of thermoelectric legs (A), module Seebeck coefficient (α), resistance (R), module electrical conductivity (σ), module thermal conductivity (κ), module figure of merit (ZT), power generated (P_e), maximum power generated ($P_{e,max}$), and efficiency (η).

$$R = \frac{V_O - V_S}{I_O - I_S} \tag{28}$$

$$\alpha = \frac{V_O}{T_H - T_C} \tag{29}$$

$$\kappa = \frac{\frac{q_{H,Measured}}{T_H - T_C} \times l}{A} \tag{30}$$

$$\sigma = \frac{l}{R \times A} \tag{31}$$

$$q_{H,calc} = \alpha T_H I_S + \kappa (T_H - T_C) - \frac{I_S^2 R}{2} \tag{32}$$

$$q_C = \alpha T_C I_S + \kappa (T_H - T_C) - \frac{I_S^2 R}{2} \tag{33}$$

$$P_{e,\max} = \frac{\alpha^2 (T_H - T_C)^2}{4R} \tag{34}$$

$$\eta = \frac{P_{e,\max}}{q_{H,Measured}} \tag{35}$$

C. Fabrication Methods

Legs ~4x4x10mm of $Ga_2In_6Sn_2O_{16}$, $Ca_{2.93}Sr_{0.07}Co_4O_9$ were cut. *P-n* couples were made in the following manner: Ag-paste (Sigma Aldrich) was painted on the top and bottom of the legs, Ag-foil (Sigma Aldrich) was connected to the legs and then more Ag-paste was applied to an alumina substrate (Coorstek, Boulder, CO). The parts were then dried at 130°C for 1hr to remove organics. Then the unit was heated to 850°C for 2hr under uniaxial pressure to increase contact between the legs and the electrodes. Ag-foil was extended on the determined "cold side" in order to allow for electrical connections while testing. Figure 44 shows a final TEG, and a TEG after final firing with the cold side substrate removed.

(a)

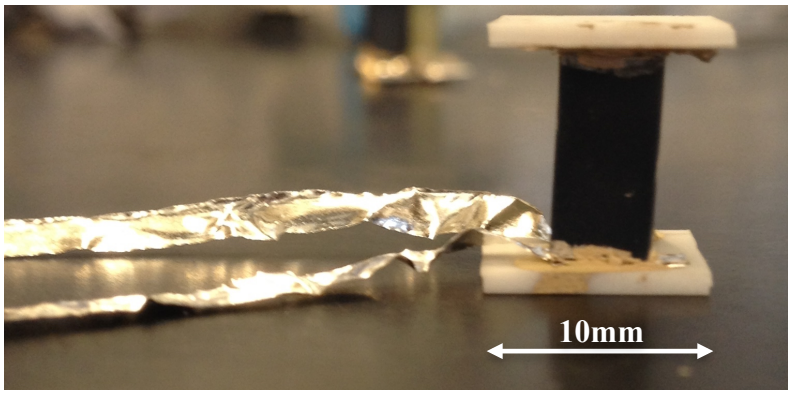

(b)

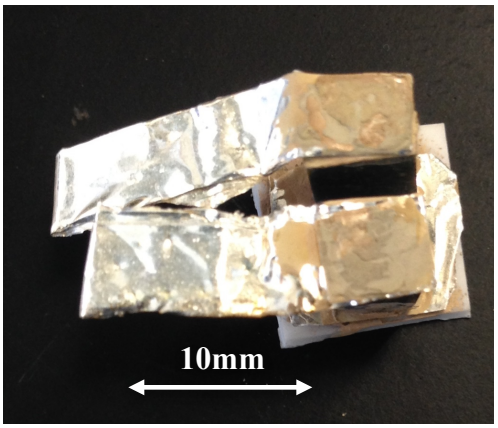

Figure 44 Photographs of TEG from a) bottom side view and b) top view with substrate removed.

D. Results and Discussion

1. CTE of Thermoelectric Legs

The coefficient of thermal expansion for the thermoelectric materials used in the TEGs is recorded in Table X. Differences in CTE can lead to increased stresses in the material and decrease the contact area with the Ag-foil connections. The $Ga_2In_6Sn_2O_{16}$ had about a three-fold larger CTE than the $Ca_{2.93}Sr_{0.07}Co_4O_9$. Since the TEG was tested under pressure, any decrease in contact area during testing should be minimal even though there is a large difference in CTE.

Table X. Linear Coefficient of Thermal Expansion for Materials Used in Thermoelectric Generators; For Each Material, N-type or P-type is Noted

Material	$Ga_2In_6Sn_2O_{16}$	$Ca_{2.93}Sr_{0.07}Co_4O_9$
N-type or P-type	n-type	p-type
CTE	15.62ppm	5.53ppm

2. SEM of TEG Legs

Images of the interface of the thermoelectric legs and silver paste can be seen in Figure 45. Images were taken after testing to determine the approximate amount of silver that diffused into the thermoelectric legs. No microstructure differences can be identified from the SEM images. Overall the silver paste seems to be sitting on top of the thermoelectric material with minimal diffusion. The silver also did not seem to go into the open pores on the surface of the thermoelectric legs. No EDS was performed to determine possible diffusion.

(a) 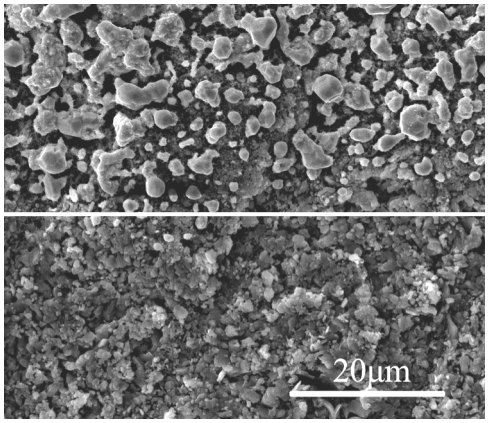

(b) 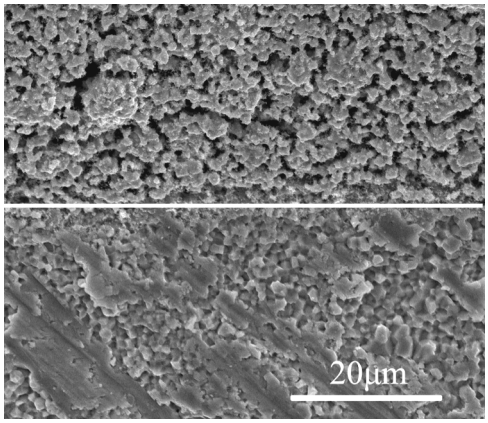

Figure 45. SEM images of (a) n-type and (b) p-type legs with silver paste. White line indicates interface of Ag paste and thermoelectric leg.

3. Testing Results and Discussion

From the measurements taken, the measured parameters and the calculated results of the TEG can be calculated, and are shown in Table XI and Table XII, respectively. Measured parameters include cold side temperature (T_C), hot side temperature (T_H), temperature difference (ΔT), and hot side heat flow ($q_{H,measured}$). Calculated resulting values include module Seebeck coefficient (α), resistance (R), module electrical conductivity (σ), module thermal conductivity (κ), module figure of merit (ZT), hot side heat flow ($q_{H,calc}$), cold side heat flow (q_C), power generated (P_e), power generated ($P_{e,\,max}$), and efficiency (η).

Table XI. Parameters Measured for Thermoelectric Generator

Parameter	Test 1	Test 2
T_C	206°C	222°C
T_H	396°C	790°C
ΔT	190°C	568°C
q_H	2.23W	7.71W

Table XII. Calculated Values for Thermoelectric Generator

Parameter	Test 1	Test 2
α	143μV/K	179μV/K
R	154mΩ	163mΩ
q_H	2.23W	2.23W
q_C	7.71W	7.71W
P_e	0.069mW	0.964mW
P_{max}	1.19mW	15.82mW
η	0.05%	0.21%
σ	13.4S/cm	12.7S/cm
κ	2.45	2.81
ZT	7.52×10^{-3}	15.4×10^{-3}

Despite CTE mismatch, the thermoelectric generator was able to mechanically sustain both temperature differences tested. The Seebeck coefficient measured in device testing is similar to that measured for the individual materials, i.e. within 72% of the predicted total Seebeck coefficient from lab measured values. The resistance is high; therefore the electrical conductivity is low, compared to that measured for the individual materials. This is most likely due to a large amount of contact resistance at the points where the thermoelectric legs are connected with the silver paste and foil to the alumina substrate. The overall module resistance can be broken down into contact resistance and the resistance from the *p* and *n*-type legs, as seen in Equation 37. From this equation, Equation 38 can be used to determine the average contact resistance from the four contacts that are made in the TEG. When the hot side temperature is 800°C, the contact resistance is 139mΩ, which is over 85% of the measured module resistance.

$$R_M = 4R_C + \left(\frac{l}{A\sigma}\right)_p + \left(\frac{l}{A\sigma}\right)_n \tag{37}$$

$$4R_C = R_M + \left(\frac{l}{A\sigma}\right)_p + \left(\frac{l}{A\sigma}\right)_n \tag{38}$$

Thermal conductivity is still lower than 5W/m*K, which means that the added silver and alumina to the TEG did not alter the module thermal conductivity. Due to the testing being completed in an argon atmosphere, it is not known if the pO_2 content caused any change in the electrical properties of the p-type material. Since thermopower, electrical conductivity, and thermal conductivity were measured on a module basis and thus only one value for each, the figure or merit equation used for thermoelectric materials can be used to determine the figure of merit values for the TEG. Due to the low electrical conductivity values from the high contact resistance, the ZT and η values were very low. The maximum η can be 53%, due to the limit of the Carnot efficiency (T_H-T_C /T_H), but the limits of ZT greatly diminishes that value. Another factor that diminished efficiency is the thermal bypass losses due to the heat lost from radiation between the two substrates. Equation 39 can give a general idea of the losses (q_{bypass}) by knowing the contact area (A), Stafan-Boltzmann contstant (s), the hot and cold side temperatures (T_H, T_C), and assuming an emissivity (ε) of 0.5.

$$q_{bypass} \approx \frac{As(T_H^{\,4} - T_C^{\,4})}{\frac{2}{\varepsilon} - 1} \tag{39}$$

When calculating the thermal bypass of the TEG when the hot side temperature is 800°C, the losses are approximately 1.6W, which may seem small but when the q_H=7.7W it is a noticeable portion of the heat flow being lost.

The power produced from one leg pair is less than 1mW, but the maximum power that can be produced is over 15mW showing that overall the TEG has much room to improve to generate maximum power. Also by making modules with more leg pairs, the overall power generated will increase. Overall the TEG that was fabricated had a major flaw of high contact resistance, but the TEG does show that it is possible to create simple devices from thermoelectric materials to produce power from waste heat applications.

CONCLUSIONS

Three thermoelectric compositions of n-type $Ga_{3-x}In_{5+x}Sn_2O_{16}$, were synthesized using solid state techniques and then consolidated using either pressureless or spark plasma sintering. Comparisons of thermoelectric properties for $Ga_{3-x}In_{5+x}Sn_2O_{16}$ using pressureless to spark plasma sintering consolidation were completed from 200°C-1000°C. Seebeck coefficient was negative, indicating an n-type thermoelectric. The electrical conductivity of SPS samples was higher than pressureless sintered samples due to increased density. Figure of merit (ZT) ranged from 0.23 to 0.46 for the pressureless sintered samples and from 0.08 to 1.12 for the SPS samples at 1000°C.

The thermoelectric properties of $Ca_{3-x}Sr_xCo_4O_9$, and $Ca_{3-y}Ag_yCo_4O_9$ were sintered at different temperatures were compared. Seebeck coefficient, electrical conductivity, and thermal conductivity were measured from 200°C-800°C. Seebeck coefficient was positive, indicating hole-type conduction. Electrical and thermal conductivity were affected by doping, but did not have any distinguishable trend for either sintering temperature. The doped compositions had ZT values ranging from 0.07 to 0.6, and undoped samples had ZT values ranging from 0.25 to 0.6 at 800°C.

The simple one-leg thermoelectric generator was fabricated from n-type $Ga_2In_6Sn_2O_{16}$ and p-type $Ca_{2.93}Sr_{0.07}Co_4O_9$ legs. The measured power generation was less than 1mW, largely due to losses associated with a high contact resistance. The resulting efficiency of 0.21% when the hot side temperature was set at 800°C. Efforts to decrease contact resistance and increase the number of legs in the TEG are expected to result in improved device performance.

FUTURE WORK

Different experiments can be taken to investigate *n*-type $Ga_{3-x}In_{5+x}Sn_2O_{16}$ further. An in-depth look into the SPS series of compositions to see if x=1.0 is a maximum in thermoelectric properties or if there is another composition that has very favorable thermoelectric properties. Also by looking into other processing techniques, such as hot pressing or sintering in an inert atmosphere, which will increase electrical conductivity but may not necessarily increase thermal conductivity.

One of the main concerns using $Ca_3Co_4O_9$ in solid state synthesis in this work is how to process it to create homogeneous compositions. The $Ca_3Co_4O_9$ compositions that were sintered at 1100°C have many possibilities for further investigation. Completing high-temperature XRD experiments with standards to determine the rate that Co_2O_3 volatizes and creates the CoO phase to fully understand the decomposition reactions that occur at 926°C and 1026°C.

The thermoelectric generator has many different paths for future research. Using different facets of the design (ie. Leg sizes, number of legs, substrate thickness, etc.), while using the same leg materials can narrow the field for optimal fabrication parameters and decrease thermal bypass losses. Decreasing the contact resistance while maintaining the thermoelectric properties of the elements will be critical for increasing the performance of the device. An avenue of exploration is using a composite electrode paste with the thermoelectric material. Funahashi and Urata have shown that using Ag paste containing the thermoelectric oxide powder as an electrode mixture is effective in reducing the contact resistance of oxide thermoelectric generators.[57]

REFERENCES

1. U. S. Department of Energy, *Waste Heat Recovery: Technology and Opportunities in U.S. Industry*," p.p. 5. BCS, Incorporated, Washington, D.C., 2008.

2. E. Velmre, "Thomas Johann Seebeck (1770-1831)," *Proc. Est. Acad. Sci., Eng.,* **13** [4] 276-82 (2007).

3. G. J. Snyder and E. S. Toberer, "Complex thermoelectric materials." *Nat. Mater*. **7** [2] 105-114 (2008).

4. J. Yang and T. Caillat, "Thermoelectric materials for space and automotive generation," *MRS Bull.*, **31** [3] 224-9 (2006).

5. K. Koumoto, R. Funahashi, E. Guilmeau, Y. Miyazaki, A. Weidenkaff, Y. Wang, C. Wan, and X. D. Zhou, "Thermoelectric Ceramics for Energy Harvesting," *J. Am. Ceram. Soc.,* **96** [1] 1-23 (2013).

6. U. S. Department of Energy, *Waste Heat Recovery: Technology and Opportunities in U.S. Industry*," p.p. 8. BCS, Incorporated, Washington, D.C., 2008.

7. K. Koumoto, I. Terasaki, and R. Funahashi, "Complex Oxide Materials for Potential Thermoelectric Applications," *MRS Bull.,* **31** [03] 206-10 (2006).

8. T.M. Tritt and M.A. Subramanian, "Thermoelectric Materials, Phenomena, and Application: A Bird's Eye View," *Mater. Res. Bull.*, **31** [3] 188-94 (2006).

9. Pradeep Fulay, *Electronic Magnetic and Optical Material*; pp. 88-89. CRC Press (Taylor & Francis Group), Boca Raton, FL, 2010.

10. T.M. Tritt and M.A. Subramanian, "Thermoelectric Materials, Phenomena, and Application: A Bird's Eye View," *Mater. Res. Bull.*, **31** [3] 188-94 (2006).

11. G. J. Snyder and E. S. Toberer, "Complex thermoelectric materials." *Nat. Mater*., **7** [2]: 105-114 (2008).

12. D. M. Rowe, "General Principles and Basic Considerations"; pp. 1-8. in *Thermoelectrics Handbook*. CRC Press, 2005.

13. C. Kittel, "Phonons I. Crystal Vibrations," pp. 89-104 in *Intro to Solid State Physics*. John Wiley & Sons, New York, 2007.

14. G. J. Snyder and E. S. Toberer, "Complex thermoelectric materials." *Nat. Mater*., **7** [2]: 105-114 (2008).

15. M. Hamid Elsheikh, D. A. Shnawah, M. F. M. Sabri, S. B. M. Said, M. Haji Hassan, M. B. Ali Bashir, and M. Mohamad, "A review on thermoelectric renewable energy: Principle parameters that affect their performance," *Renewable Sustainable Energy Rev.,* **30** 337-55 (2014).

16. J. W. Fergus, "Oxide materials for high temperature thermoelectric energy conversion," *J. Eur. Ceram. Soc.,* **32** [3] 525-40 (2012).

17. K. Koumoto, R. Funahashi, E. Guilmeau, Y. Miyazaki, A. Weidenkaff, Y. Wang, C. Wan, and X. D. Zhou, "Thermoelectric Ceramics for Energy Harvesting," *J. Am. Ceram. Soc.,* **96** [1] 1-23 (2013).

18. I. Terasaki, Y. Sasago, and K. Uchinokura, "Large Thermoelectric Power in NaCo2O4 Single Crystals," *Phys. Rev. B.*, **56** [20] R12685-7 (1997).

19. T.M. Tritt and M.A. Subramanian, "Thermoelectric Materials, Phenomena, and Application: A Bird's Eye View," *Mater. Res. Bull.*, **31** [3] 188-94 (2006).

20. W. Koshibae and S. Maekawa, "Effects of Spin and Orbital Degeneracy on the Thermopower of Strongly Correlated Systems," *Phys. Rev. Lett.,* **87** [23] (2001).

21. K. Koumoto, I. Terasaki, and R. Funahashi, "Complex Oxide Materials for Potential Thermoelectric Applications," *MRS Bull.,* **31** [03] 206-10 (2006).

22. "Standard Test Method for Water Adsorption, Bulk Density, Apparent Porosity, and Apparent Specific Gravity of Fired Whiteware Products," ASTM C373-88 (1999). American Society of Testing and Materials, West Conshohocken, PA.

23. A. Trestman-Matts, S.E. Dorris, and T.O. Mason, "Measurement and Interpretation of Thermopower in Oxides," *J. Am. Ceram. Soc.*, **66** [8] 589-92 (1983).

24. A.T. Burkov, "Measurements of Resistivity and Thermopower: Principles and Practical Realization," pp. 228-9 in *Thermoelectrics Handbook: Macro to Nano*. Edited by D.M. Rowe. CRC Press, Taylor & Francis Group, Boca Raton, FL, 2006.

25. W.J. Parker, R.J. Jenkins, C.P. Butler, and G.L. Abbott, "Flash Methos of Determining Thermal Diffusivity, Heat Capacity, and Thermal Conductivity," *J. Appl. Phys.*, **32** [9] 1679-84 (1961).

26. M.A. Thermitus and P.S. Gaal, "Thermal Diffusivity and the Flash Method Technical Note 68B," Anter Corporation, Pittsburgh, PA, 2007 (unpublished).

27. D. D. Edwards, T.O. Mason, W. Sinkler, L. D. Marks, K.R. Poeppelmeier, Z. Hu, and J.D. Jorgensen "Tunneled Intergrowth Structures in the Ga_2O_3-In_2O_3-SnO_2 System," *J. Solid State Chem.,* **150** 294-304 (2000).

28. D. D. Edwards, T. O. Mason, F. Goutenoire, and K. R. Poeppelmeier, “A New Transparent Conducting Oxide in the Ga_2O_3-In_2O_3-SnO_2 System,” *Appl. Phys. Lett.* **70** 1706–1708 (1997).

29. A. Dolgonos, K. Lam, K. R. Poeppelmeier, A. J. Freeman, and T. O. Mason, "Electronic and optical properties of Ga3−xIn5+xSn2O16: An experimental and theoretical study," *J. Appl. Phys.,* **115** [1] 013703 (2014).

30. S. D. Bhame, T. Zhou, E. Guilmeau, Y. Kinemuchi, F. Delorme, and B. Raveau, "Synthesis and thermoelectric properties of oxygen deficient fluorite derivative Ga3−xIn5+xSn2O16," *J. Appl. Phys.,* **108** [9] 093708 (2010).

31. D. D. Edwards, T.O. Mason, W. Sinkler, and L. D. Marks, "A Structural Investigation of Ga3+xIn5-xSn2O16," *J. Solid State Chem.,* **140** 242-50 (1998).

32. A. Dolgonos, K. Lam, K. R. Poeppelmeier, A. J. Freeman, and T. O. Mason, "Electronic and optical properties of Ga3−xIn5+xSn2O16: An experimental and theoretical study," *J. Appl. Phys.,* **115** [1] 013703 (2014).

33. S. D. Bhame, T. Zhou, E. Guilmeau, Y. Kinemuchi, F. Delorme, and B. Raveau, "Synthesis and thermoelectric properties of oxygen deficient fluorite derivative Ga3−xIn5+xSn2O16," *J. Appl. Phys.,* **108** [9] 093708 (2010).

34. S. D. Bhame, T. Zhou, E. Guilmeau, Y. Kinemuchi, F. Delorme, and B. Raveau, "Synthesis and thermoelectric properties of oxygen deficient fluorite derivative Ga3−xIn5+xSn2O16," *J. Appl. Phys.,* **108** [9] 093708 (2010).

35. S. D. Bhame, T. Zhou, E. Guilmeau, Y. Kinemuchi, F. Delorme, and B. Raveau, "Synthesis and thermoelectric properties of oxygen deficient fluorite derivative Ga3−xIn5+xSn2O16," *J. Appl. Phys.,* **108** [9] 093708 (2010).

36. S. Li, R. Funahashi, I. Matsubara, H. Yamada, K. Ueno, and S. Sodeoka, "Synthesis and thermoelectric properties of the new oxide ceramics Ca3−xSrxCo4O9+δ (x=0.0–1.0)," *Ceram. Int.,* **27** [3] 321-24 (2001).

37. W. Tao, A. T. Trevor, C. Haiyan, B. Jianming, W. Hsin, and J. Cherno, "A structural change in Ca 3 Co 4 O 9 associated with enhanced thermoelectric properties," *J. Phys.: Condens. Matter,* **24** [45] 455602 (2012).

38. E. Woermann and A. Muan, "Phase equilibria in the system CaO-cobalt oxide in air," *J. Inorg. Nucl. Chem.,* **32** [5] 1455-59 (1970).

39. G. Constantinescu, S. Rasekh, M. A. Torres, J. C. Diez, M. A. Madre, and A. Sotelo, "Effect of Sr substitution for Ca on the Ca3Co4O9 thermoelectric properties," *J. Alloys Compd.,* **577** 511-15 (2013).

40. J. W. Fergus, "Oxide materials for high temperature thermoelectric energy conversion," *J. Eur. Ceram. Soc.,* **32** [3] 525-40 (2012).

41. S. Li, R. Funahashi, I. Matsubara, H. Yamada, K. Ueno, and S. Sodeoka, "Synthesis and thermoelectric properties of the new oxide ceramics Ca3−xSrxCo4O9+δ (x=0.0–1.0)," *Ceram. Int.,* **27** [3] 321-24 (2001).

42. F. Delorme, C. F. Martin, P. Marudhachalam, D. Ovono Ovono, and G. Guzman, "Effect of Ca substitution by Sr on the thermoelectric properties of Ca3Co4O9 ceramics," *J. Alloys Compd.,* **509** [5] 2311-15 (2011).

43. J. W. Fergus, "Oxide materials for high temperature thermoelectric energy conversion," *J. Eur. Ceram. Soc.,* **32** [3] 525-40 (2012).

44. Y. Zhou, I. Matsubara, S. Horii, T. Takeuchi, R. Funahashi, M. Shikano, J.-i. Shimoyama, K. Kishio, W. Shin, N. Izu, and N. Murayama, "Thermoelectric properties of highly grain-aligned and densified Co-based oxide ceramics," *J. Appl. Phys.,* **93** [5] 2653 (2003).

45. A. Sotelo, G. Constantinescu, S. Rasekh, M. A. Torres, J. C. Diez, and M. A. Madre, "Improvement of thermoelectric properties of Ca3Co4O9 using soft chemistry synthetic methods," *J. Eur. Ceram. Soc.,* **32** [10] 2415-22 (2012).

46. H. Tran, T. Mehta, M. Zeller, and R. H. Jarman, "Synthesis and characterization of mixed phases in the Ca–Co–O system using the Pechini method," *Maert. Res. Bull.,* **48** [7] 2450-56 (2013).

47. Y. Zhang and J. Zhang, "Rapid reactive synthesis and sintering of textured Ca3Co4O9 ceramics by spark plasma sintering," *J. Mater. Process. Technol.,* **208** [1-3] 70-74 (2008).

48. G. Constantinescu, S. Rasekh, M. A. Torres, J. C. Diez, M. A. Madre, and A. Sotelo, "Effect of Sr substitution for Ca on the Ca3Co4O9 thermoelectric properties," *J. Alloys Compd.,* **577** 511-15 (2013).

49. G. Constantinescu, S. Rasekh, M. A. Torres, J. C. Diez, M. A. Madre, and A. Sotelo, "Effect of Sr substitution for Ca on the Ca3Co4O9 thermoelectric properties," *J. Alloys Compd.,* **577** 511-15 (2013).

50. Y. Wang, Y. Sui, J. Cheng, X. Wang, and W. Su, "Comparison of the high temperature thermoelectric properties for Ag-doped and Ag-added Ca3Co4O9," *J. Alloys Compd.,* **477** [1-2] 817-21 (2009).

51 F. P. Zhang, Q. M. Lu, and J. X. Zhang, "Synthesis and high temperature thermoelectric properties of BaxAgyCa3−x−yCo4O9 compounds," *J. Alloys Compd.,* **484** [1-2] 550-54 (2009).

52. S. Li, R. Funahashi, I. Matsubara, H. Yamada, K. Ueno, and S. Sodeoka, "Synthesis and thermoelectric properties of the new oxide ceramics Ca3−xSrxCo4O9+δ (x=0.0–1.0)," *Ceram. Int.,* **27** [3] 321-24 (2001).

53. J. W. Fergus, "Oxide materials for high temperature thermoelectric energy conversion," *J. Eur. Ceram. Soc.,* **32** [3] 525-40 (2012).

54. S.-M. Choi, K.-H. Lee, C.-H. Lim, and W.-S. Seo, "Oxide-based thermoelectric power generation module using p-type Ca3Co4O9 and n-type (ZnO)7In2O3 legs," *Energy Convers. Manage.,* **52** [1] 335-39 (2011).

55. I. Matsubara, R. Funahashi, T. Takeuchi, S. Sodeoka, T. Shimizu, and K. Ueno, "Fabrication of an all-oxide thermoelectric power generator," *Appl. Phys. Lett.,* **78** [23] 3627 (2001).

56. J. G. Noudem, S. Lemonnier, M. Prevel, E. S. Reddy, E. Guilmeau, and C. Goupil, "Thermoelectric ceramics for generators," *J. Eur. Ceram. Soc.,* **28** [1] 41-48 (2008).

[57] R. Funahashi and S. Urata, "Fabrication and Application of an Oxide Thermoelectric System," *Int. J. Appl. Ceram. Technol.,* **4** [4] 297-307 (2007).